Electronic Supplementary Information (ESI†) for

Modulated synthesis of thiol-functionalized fcu- and hcp-UiO-66(Zr) for the removal of silver(I) ions from water

Bastian Moll, Tim Müller, Carsten Schlüsener, Alexa Schmitz, Philipp Brandt, Secil Öztürk, Christoph Janiak

Institut für Anorganische Chemie und Strukturchemie, Heinrich-Heine-Universität, D-40204 Düsseldorf, Germany

Email addresses: bastian.moll@hhu.de, T.Mueller@uni-duesseldorf.de, carsten.schluesener@uni-duesseldorf.de, alexa.schmitz@uni-duesseldorf.de, p.brandt@uni-duesseldorf.de, oeztues@uni-duesseldorf.de, janiak@uni-duesseldorf.de

Table of content

S1 Synthesis parameters

Table S1 Molar ratios and mass for UiO-66-MAc-10eq, -30eq, -50eq and hcp UiO-66-MAc-100eq.

| UiO-66-MAc-Xeq	m $ZrCl_4$ [mg]	n $ZrCl_4$ [mmol]	m H_2BDC [mg]	n H_2BDC [mmol]	ratio H_2BDC: ZrCl4	V HMAc [ml]	n HMAc [mmol]	ratio HMAc: $ZrCl_4$
10eq	206.80	0.90	161.0	1.10	1.10	0.70	10.10	11.30
30eq	229. 00	1.00	170.0	1.00	1.00	2.00	28.80	29.90
50eq	231.30	0.99	174.8	1.05	1.06	3.50	50.34	50.72
70eq	227.40	0.98	177.4	1.07	1.09	4.90	70.47	71.91
80eq	229.50	0.98	175.0	1.05	1.07	5.60	80.55	82.19
90eq	229.60	0.99	175.0	1.05	1.06	6.30	90.61	91.53
hcp 100eq	226.60	0.97	171.0	1.03	1.06	7.00	100.68	103.55
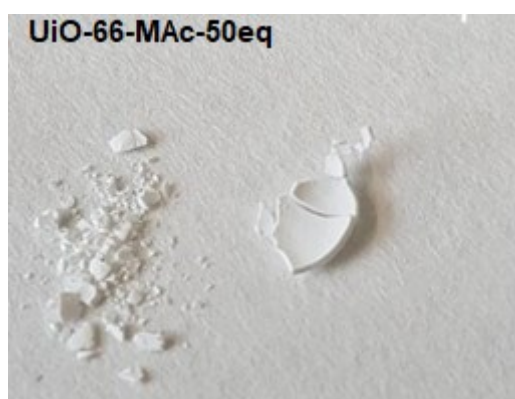
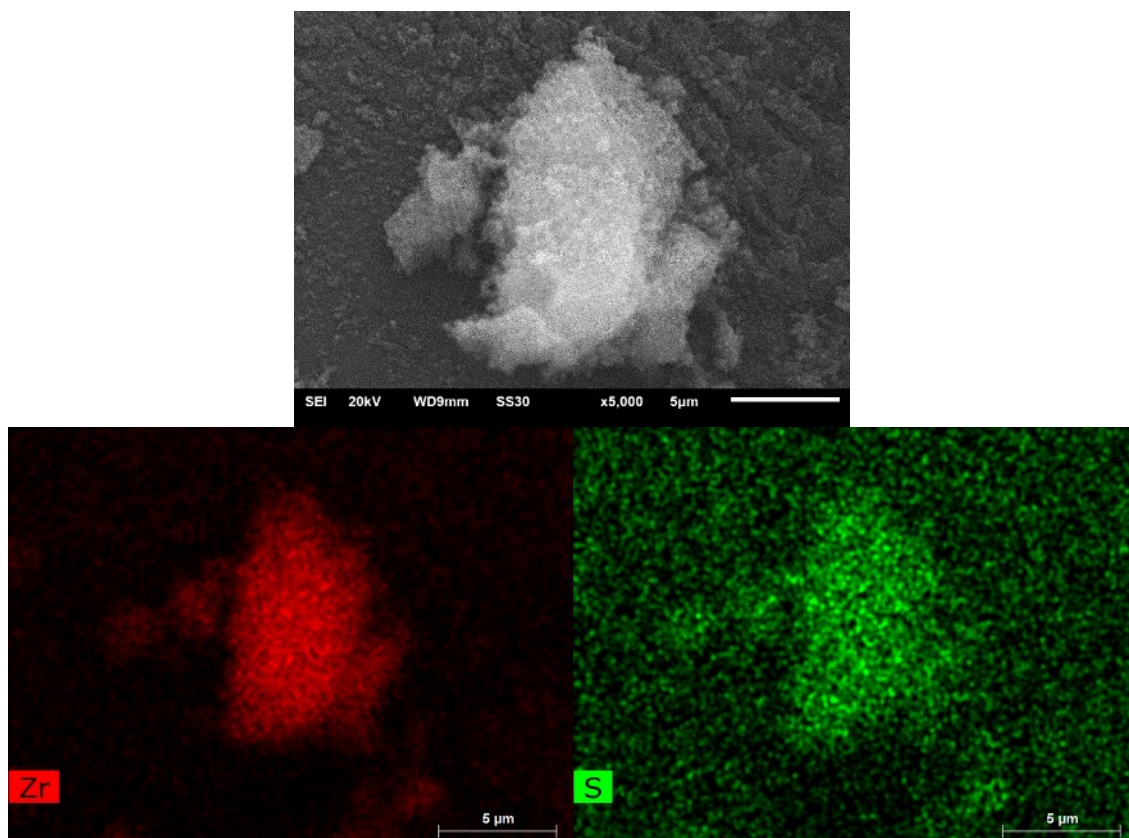**Figure S1** Picture of the synthesized UiO-66 with 50 eq of mercaptoacetic acid after drying.

S2 SEM-EDX

S2.1 SEM pictures and EDX element mapping (SEM-EDX)
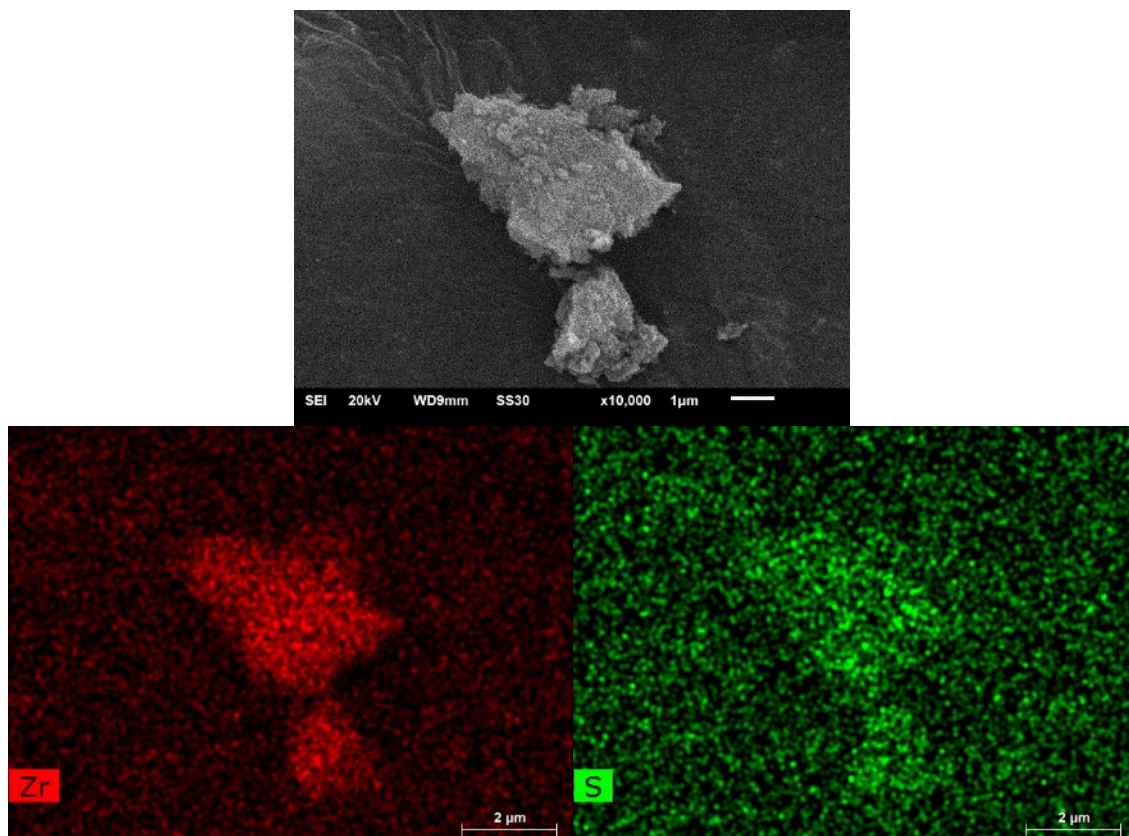
Figure S2 SEM image of agglomerated particles of UiO-66-MAc-10eq and its Zr (red) and S-(green) EDX element maps.

Figure S3 SEM image of agglomerated particles of UiO-66-MAc-30eq and its Zr (red) and S-(green) EDX element maps.
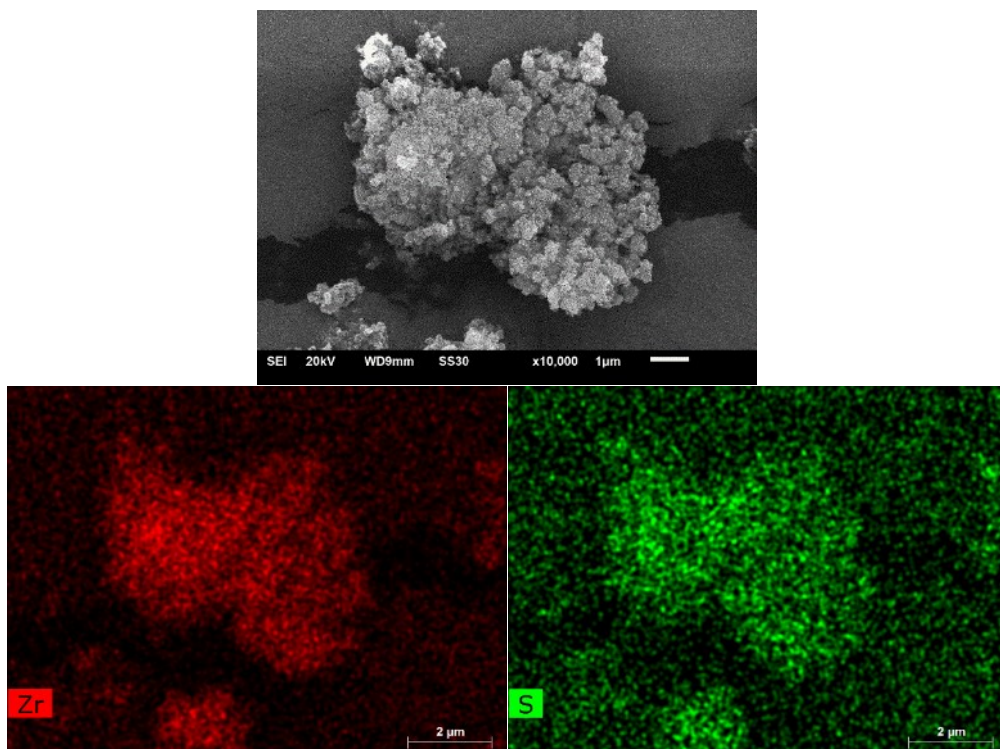
Figure S4 SEM image of agglomerated particles of UiO-66-MAc-50eq and its Zr (red) and S-(green) EDX element maps.
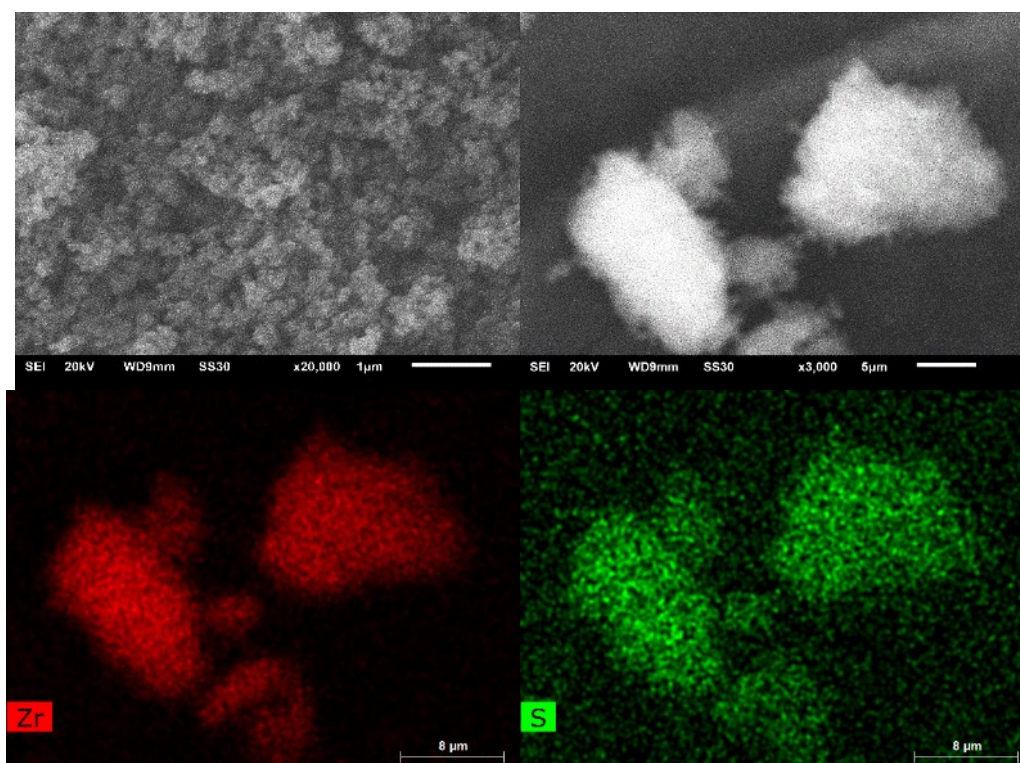

Figure S5 SEM images of agglomerated particles of UiO-66-MAc-100eq and its Zr (red) and S-(green) EDX element maps.

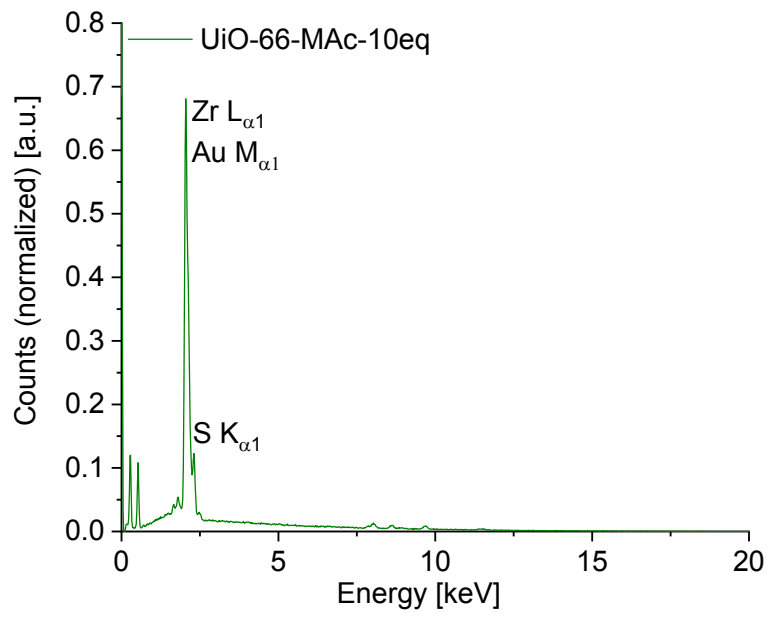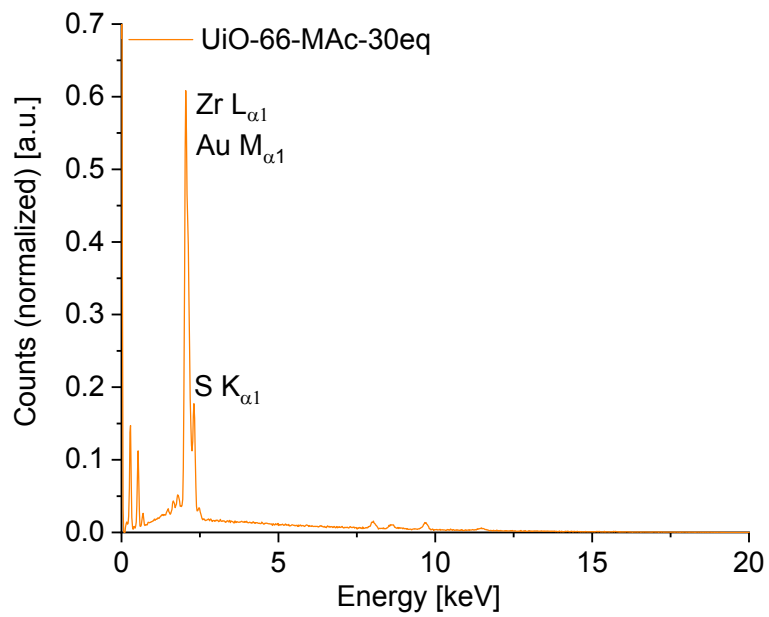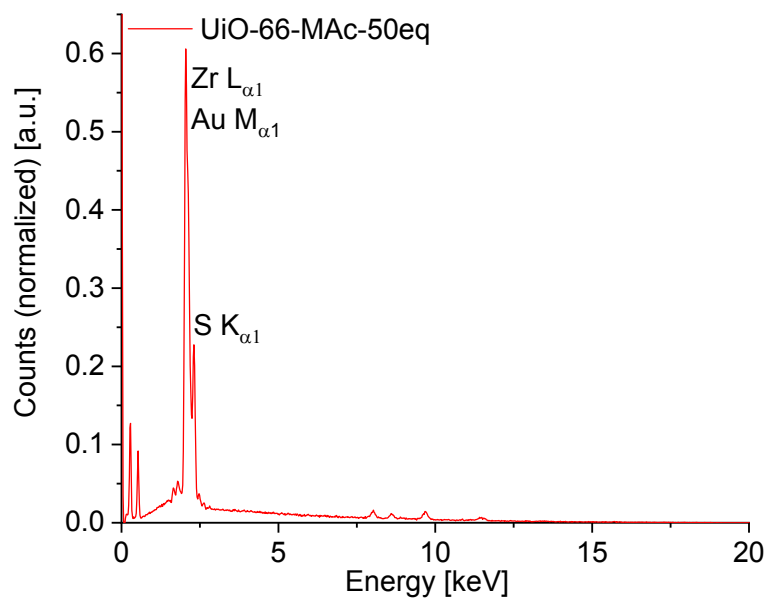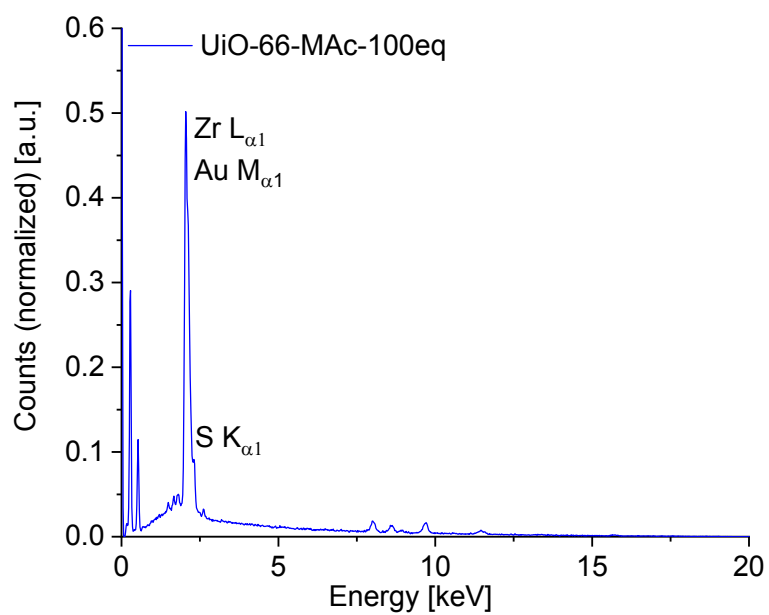**S2.2 Zirconium:sulfur ratios (Zr:S;) by SEM-EDX**

Figure S6 SEM-EDX spectrum of UiO-66-MAc-10eq.

Figure S7 SEM-EDX spectrum of UiO-66-MAc-30eq.

Figure S8 SEM-EDX spectrum of UiO-66-MAc-50eq.

Figure S9 SEM-EDX spectrum of UiO-66-MAc-100eq.

Table S2 Determination of zirconium to sulfur amount in UiO-66-MAc-x.

UiO-66-MAc	exp. ratio Zr: S from SEM-EDX	calc. ratio Zr: S from sum formula	Sum formula [a]
10eq	1: 0.28	1: 0.24	$Zr_6O_4(OH)_4(BDC)_{4.58}(MAc)_{1.42}$
30eq	1: 0.49	1: 0.36	$Zr_6O_4(OH)_4(BDC)_{3.85}(MAc)_{2.15}$
50eq	1: 0.41	1: 0.45	$Zr_6O_4(OH)_4(BDC)_{3.33}(MAc)_{2.67}$
100eq	1: 0.27	1: 0.27	$[(Zr_6O_4(OH)_4)_2(OH)_6](BDC)_{5.73}(MAc)_{3.27}$

[a] Sum formula calculated from the average linker to modulator ratios under the assumption that one BDC^{2-} linker in ideal **fcu**-UiO-66 with $[Zr_6O_4(OH)_4(BDC)_6]$ and in ideal **hcp**-UiO-66 with $[(Zr_6O_4(OH)_4)_2(OH)_6(BDC)_9]$ is replaced by two MAc^- molecules (cf. Table 1).

In the EDX spectra the signals of Zr and Au overlap under formation of one signal with S as an additional shoulder, since the energies of these three elements are almost the same. Therefore, integrals are not completely separable, resulting in a higher variance than with the other analysis methods (NMR, TGA). Compared to the ratios obtained from sum formulae which were calculated from digestion NMR (Section S3, ESI†), TGA weight loss and defect analysis (Section S4, ESI†) the values are in good accordance.

S3 Digestion NMR and elemental analysis (CHNS)

S3.1. BDC^{2-}: MAc$^-$ ratio from digestion ^{1}H NMR spectra

Since UiO-66 proved to be unstable under basic conditions in the executed stability tests, UiO-66 is best dissolved under basic conditions (Section S8, ESI†). Here a digestion precedure from Shearer *et al.* was used.[4] All samples were dissolved in 1 mol/L NaOD/D$_2$O by mixing 20 mg of dried MOF sample with 600 μL of NaOD/D$_2$O followed by ultrasonication for 5 min. After the samples were shaken for 24 h (VWR® Mini Shaker at 200 RPM), NMR spectra of UiO-66-10eq and UiO-66-30eq showed the signals for the CH$_2$ group of MAc$^-$ at 2.1 ppm, of the two CH$_2$ groups of the disulfide dithioglycolate, $^-$O$_2$C-CH$_2$-S-S-CH$_2$-CO$_2$$^-$ (Fig. S14) at 3.01-3.20 ppm and of the four protons of terephthalate at 7.7 ppm. In addition, a quartet signal at around 2.4 ppm and a triplet signal arised at around 0.9 ppm, suggesting an additional chemical reaction during the digestion step.

The NMR of the 50 eq and the 100 eq sample after 24 h in Fig. S12 and Fig. S13 showed the signals for the CH$_2$ group of MAc$^-$ at 2.1 ppm, of the two CH$_2$ groups of the disulfide dithioglycolate, $^-$O$_2$C-CH$_2$-S-S-CH$_2$-CO$_2$$^-$ (Fig. S14) at 3.01-3.20 ppm and of the four protons of terephthalate at 7.7 ppm. The were no triplet signals to be seen.
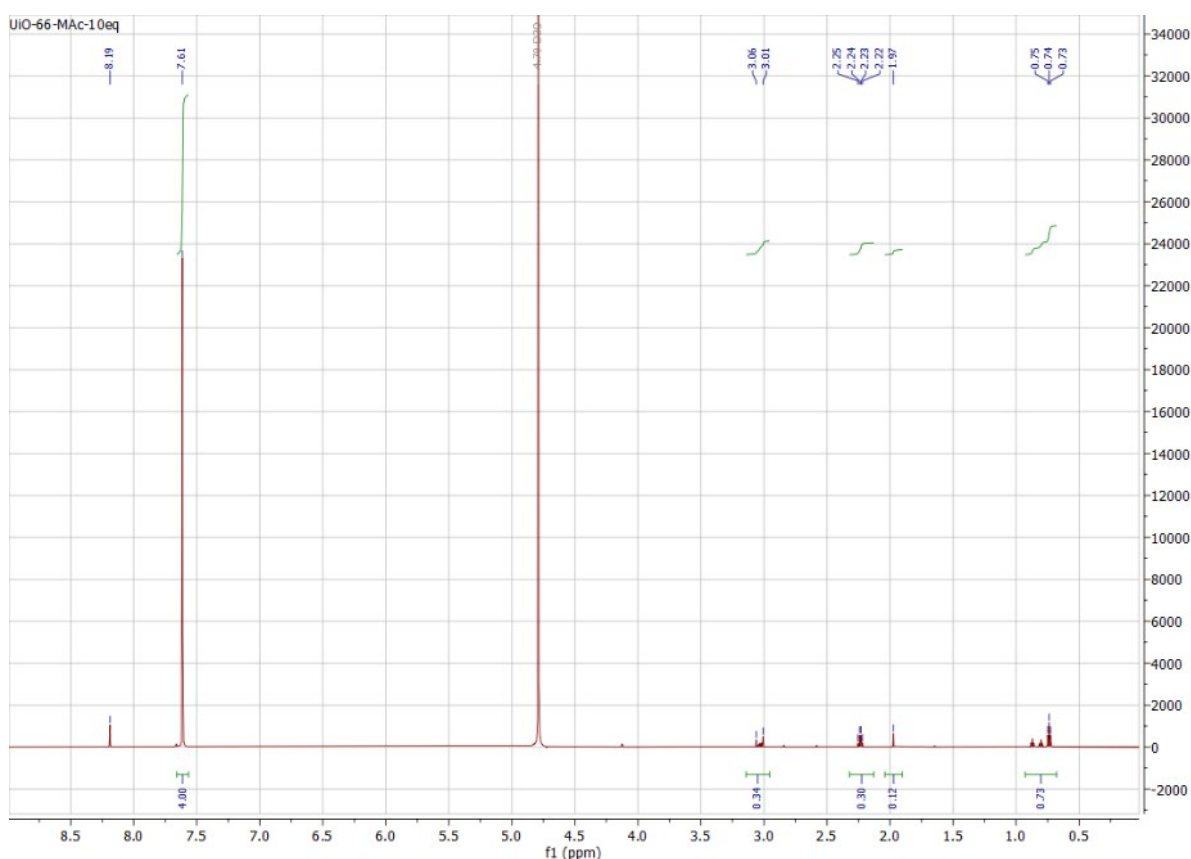
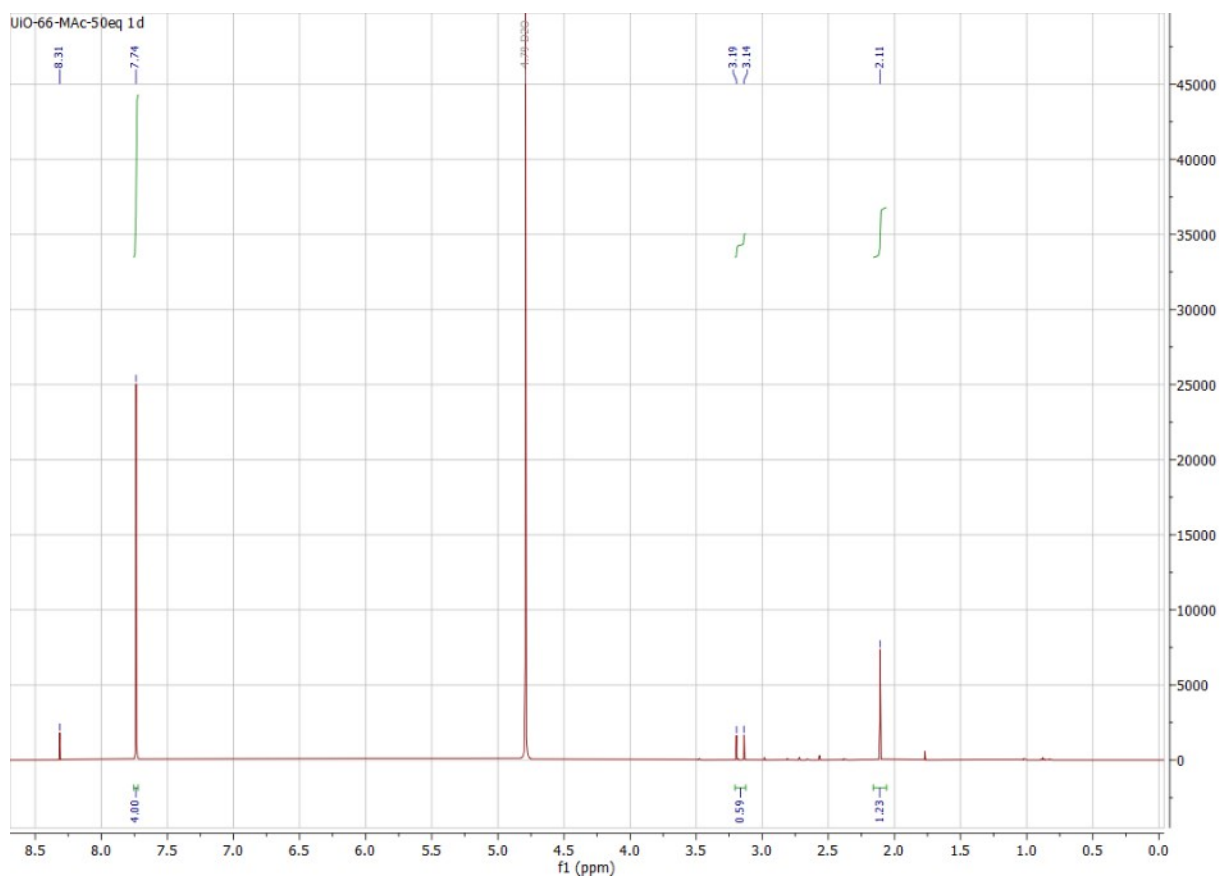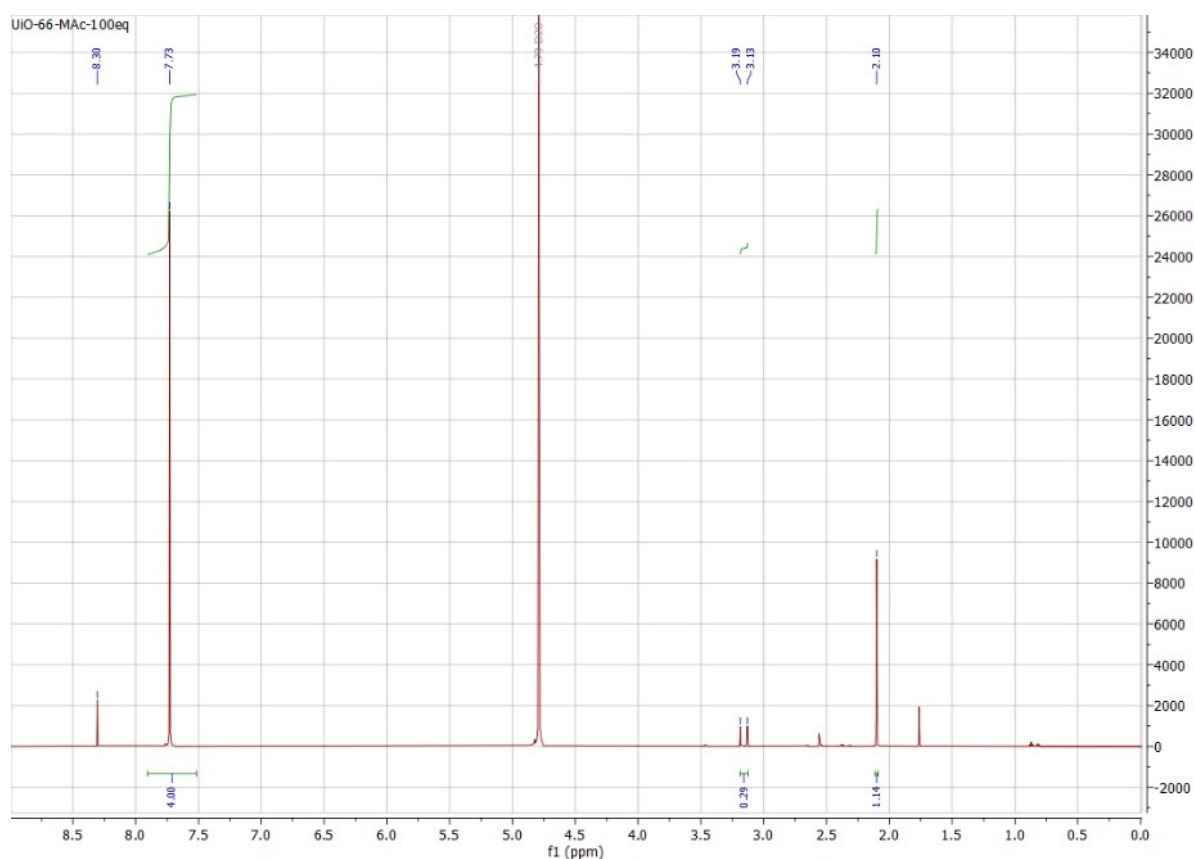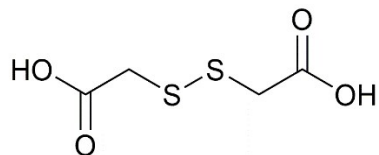**Figure S10** ^{1}H-NMR of UiO-66-MAc-10eq in NaOD/D$_2$O (c = 1 mol/L) after 24 h.
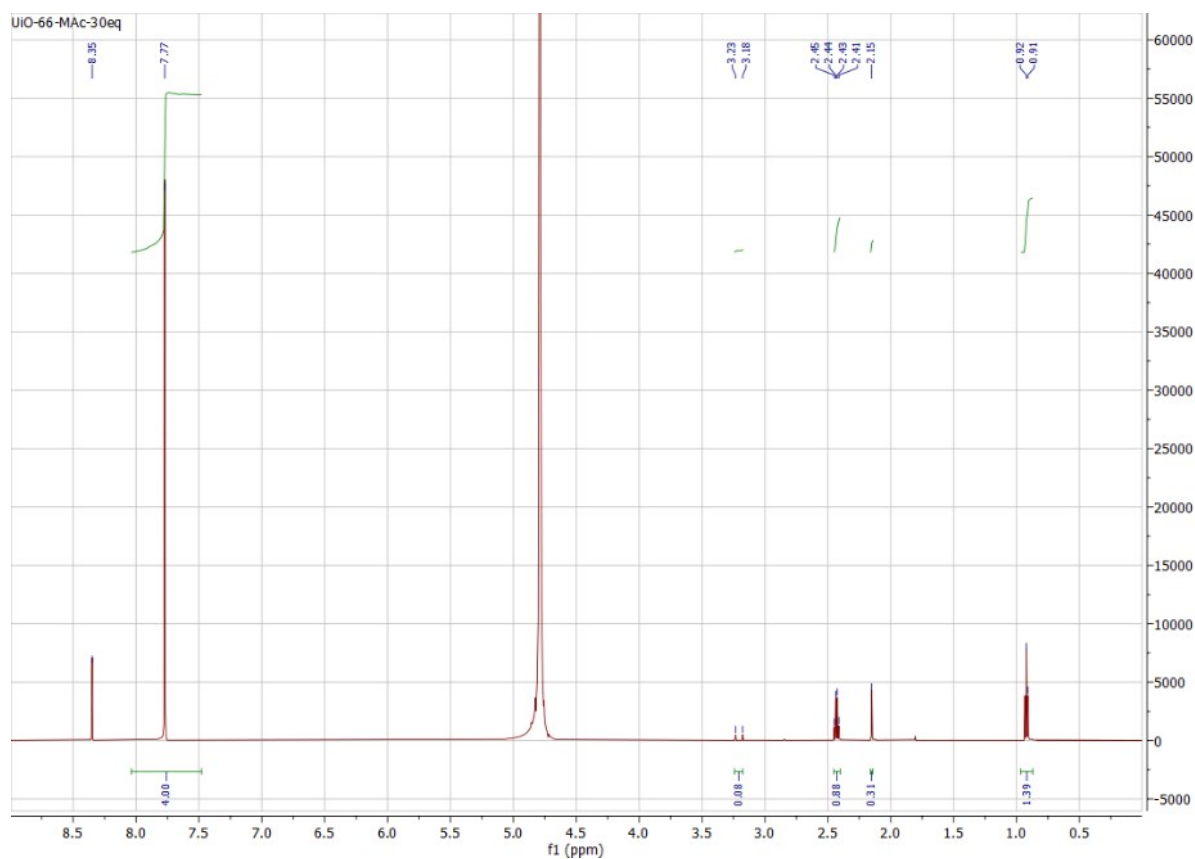
Figure S11 ^{1}H-NMR of UiO-66-MAc-30eq in NaOD/D$_2$O (c = 1 mol/L) after 24 h.

Figure S12 ^{1}H-NMR of UiO-66-MAc-50eq in NaOD/D$_2$O (c = 1 mol/L) after 24 h.

Figure S13 ^{1}H-NMR of UiO-66-MAc-100eq in NaOD/D$_2$O (c = 1 mol/L) after 24 h.

Figure S14 Dithioglycolic acid

The occurring chemical reaction during the digestion of UiO-66-MAc-10eq and -30eq was investigated under extension of the digestion time to 4 d (Fig. S16- S19). Subsequent measured NMR spectra of all materials showed the aforementioned quartet and triplet signals for the CH$_2$ group of MAc$^-$and disulfide dithioglycolate and of the four protons of the terephthalate linker. These findings indicate the formation of a mixture containing MAc$^-$, the dithioglycolate and a new reaction product.

The spectra were reproducible, showing that the reaction stopped after 4 d. Again, we assign the singlet at 2.1 ppm to the -CH$_2$ of the MAc$^-$ modulator. Notably, we observed only very small signals from the dithioglycolate at 3.01-3.20 ppm. The quartet (2.4 ppm) and triplet (0.9 ppm) signals showed a coupling constant of 7.25 Hz (using a 600 MHz NMR spectrometer) and the integral ratio for quartet to triplet is 2:3. Coupling constants, NMR splitting patterns of quartet and triplet and the integral ratio of 2:3 indicating an H$_3$C-CH$_2$-R matching with the NMR spectrum of propionic acid (Fig. S15, ^{1}H NMR spectrum see Fig. S21)

10
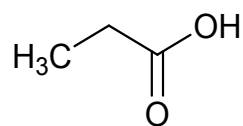
Figure S15 Propionic acid

We attribute these findings to a C-C cross coupling reaction with the dithioglycolic acid and residual or coordinated methanol in the pores of the MOFs. This reaction may be catalyzed by free Zr- ions in the decomposition solution. Transition metal catalyzed reactions of thiols and sulfides are well investigated in literature.[1,2] In 1999 Srogl *et al.* presented a transition metal catalyzed cross coupling of mercaptoacetic acid derivates, in which methyl or ethyl groups were introduced by C-C coupling.[1] Zirconium is also known for catalyzing cross coupling reactions.
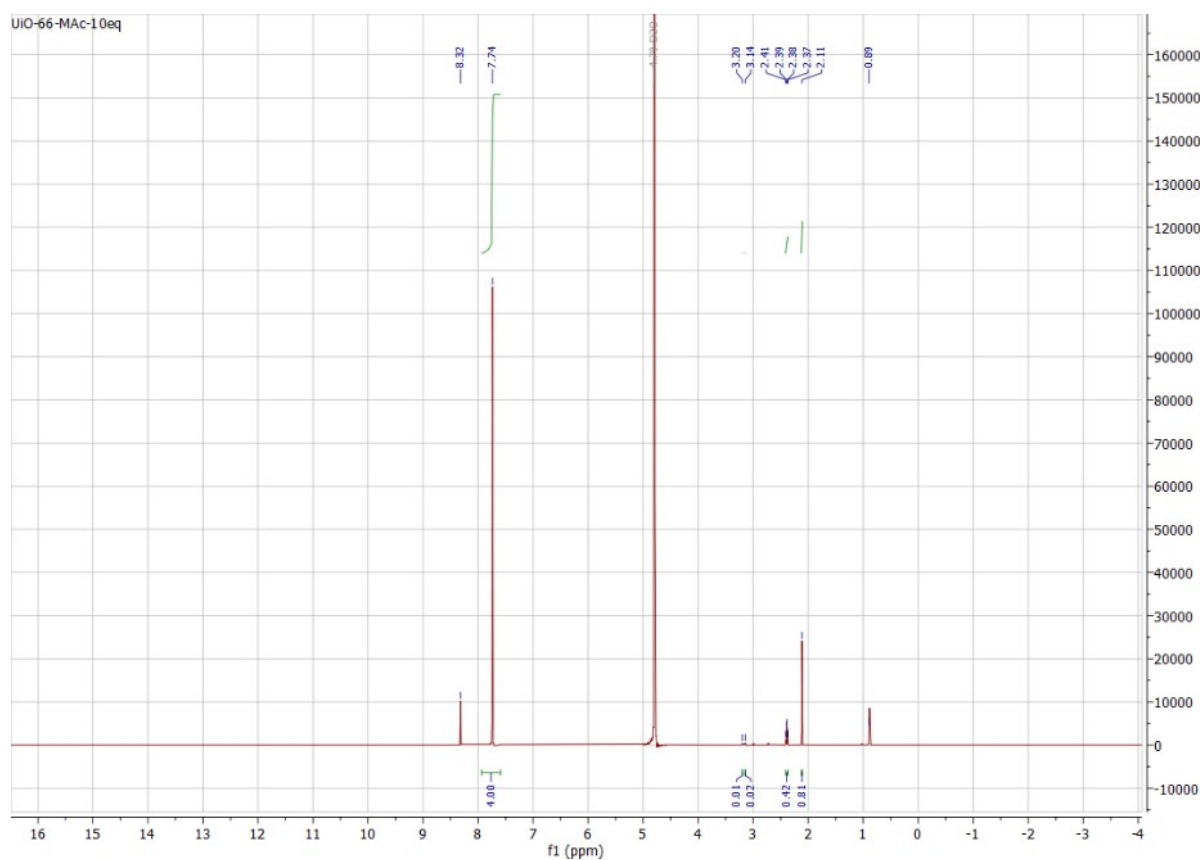
Figure S16 ^{1}H-NMR of UiO-66-MAc-10eq in NaOD/D$_2$O (c = 1 mol/L) after 4 d.
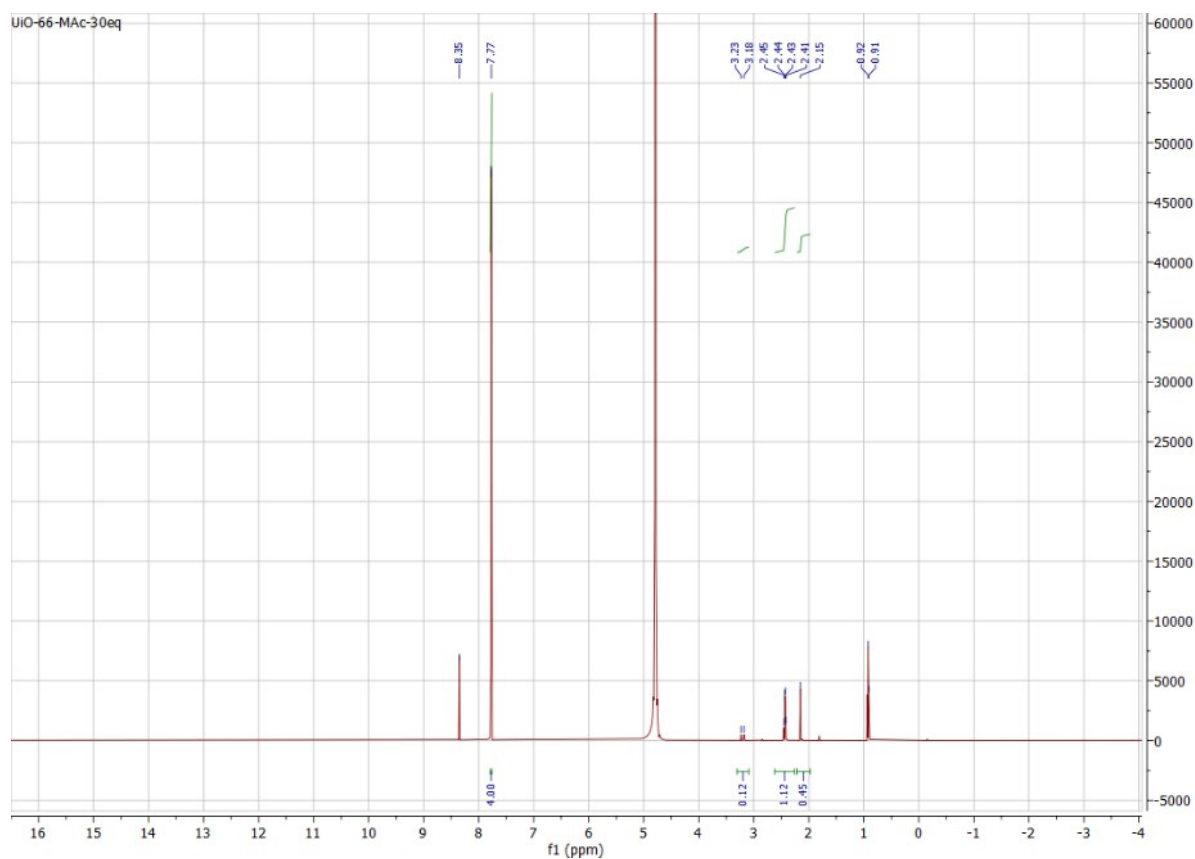
Figure S17 ^{1}H-NMR of UiO-66-MAc-30eq in NaOD/D$_2$O (c = 1 mol/L) after 4 d.
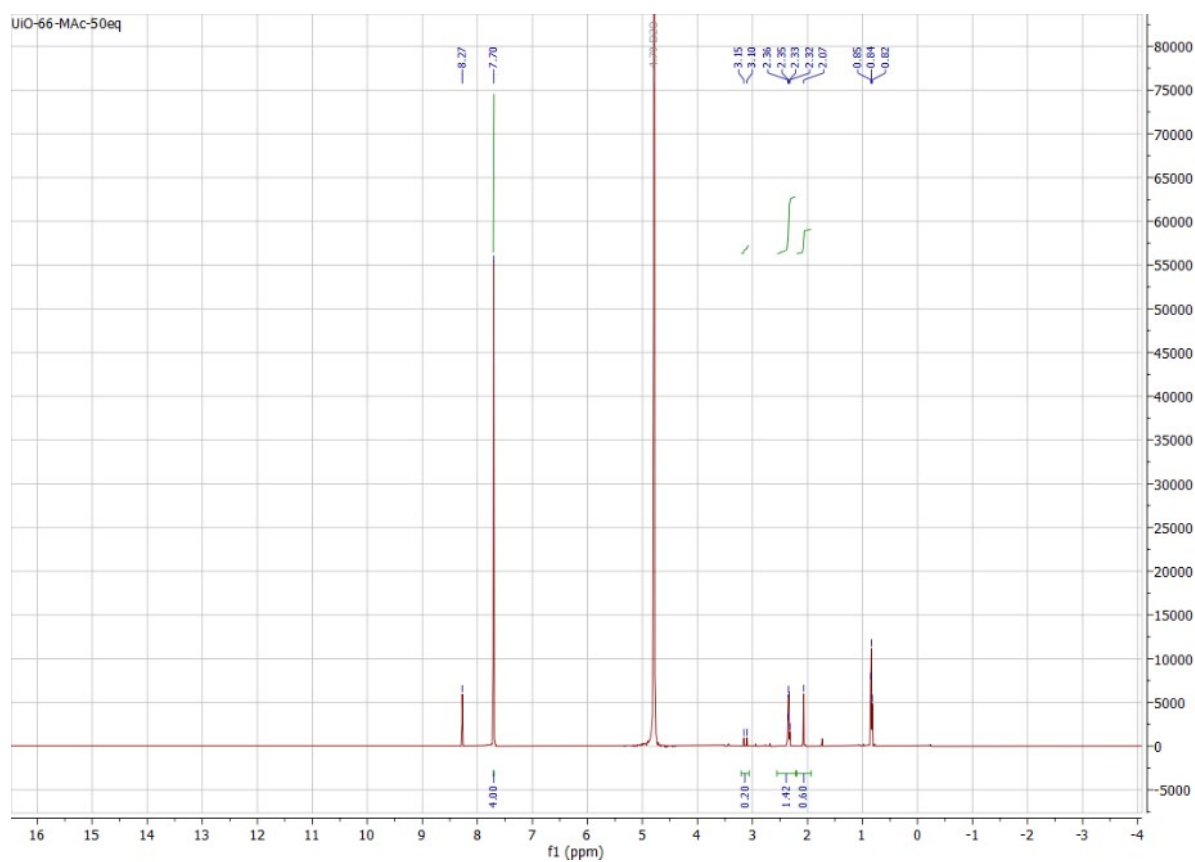
Figure S18 ^{1}H-NMR of UiO-66-MAc-50eq in NaOD/D$_2$O (c = 1 mol/L) after 4 d.
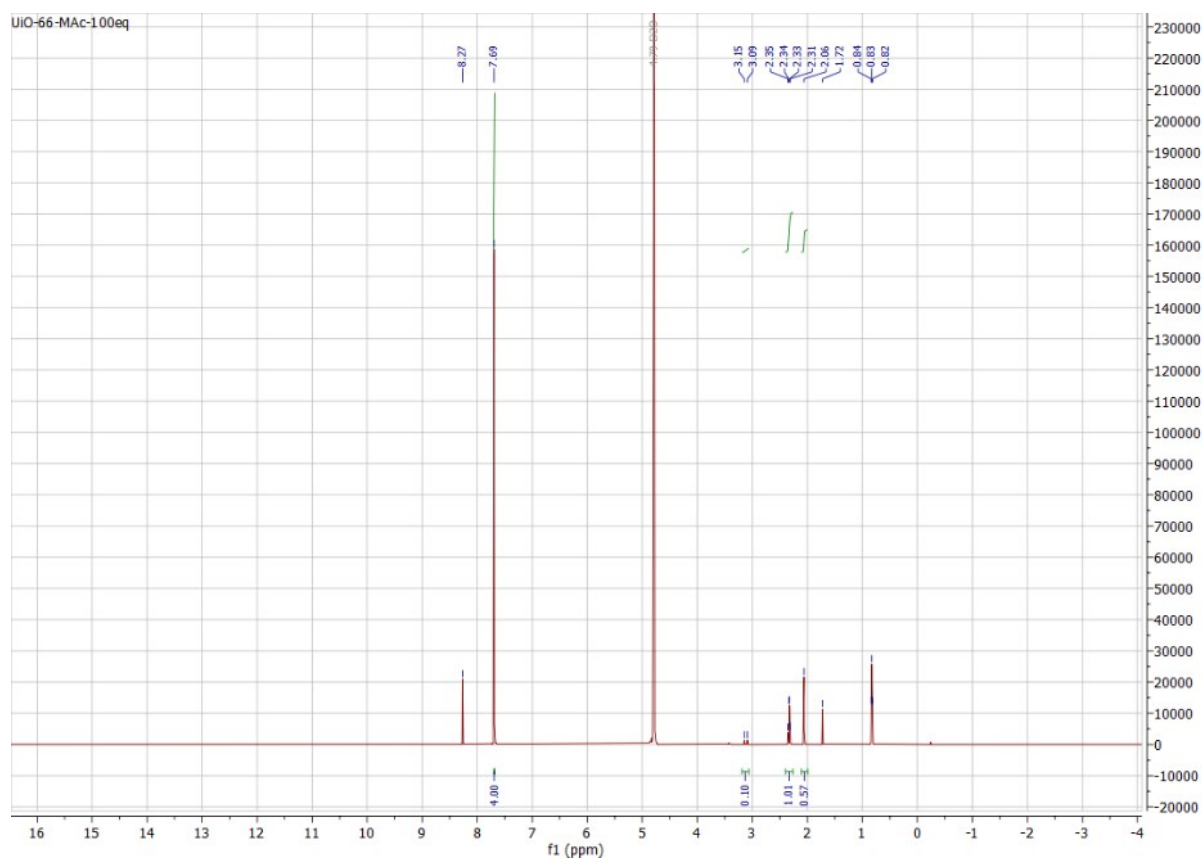
Figure S19 ^{1}H-NMR of UiO-66-MAc-100eq in NaOD/D$_2$O (c = 1 mol/L) after 4 d.
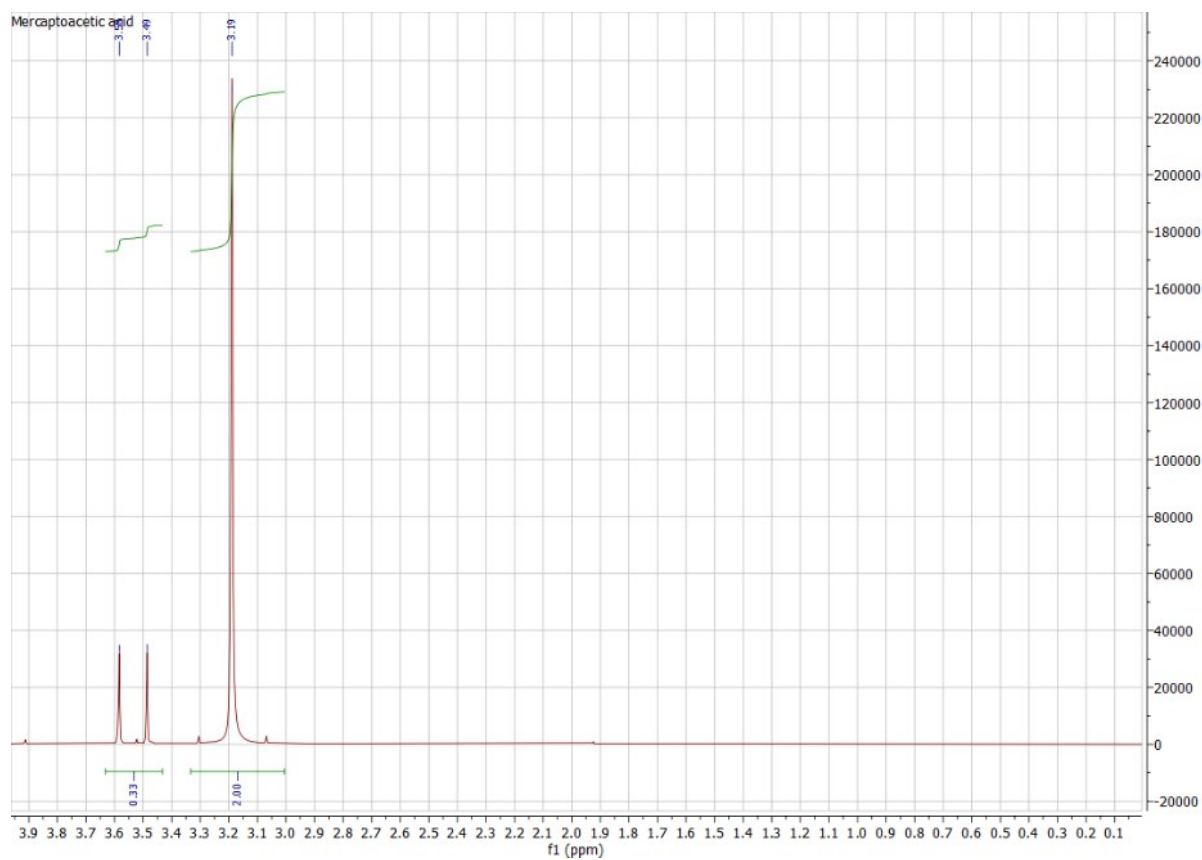
Figure S20 ^{1}H-NMR of mercaptoacetic acid (HMAc) in NaOD/D$_2$O (c = 1 mol/L)
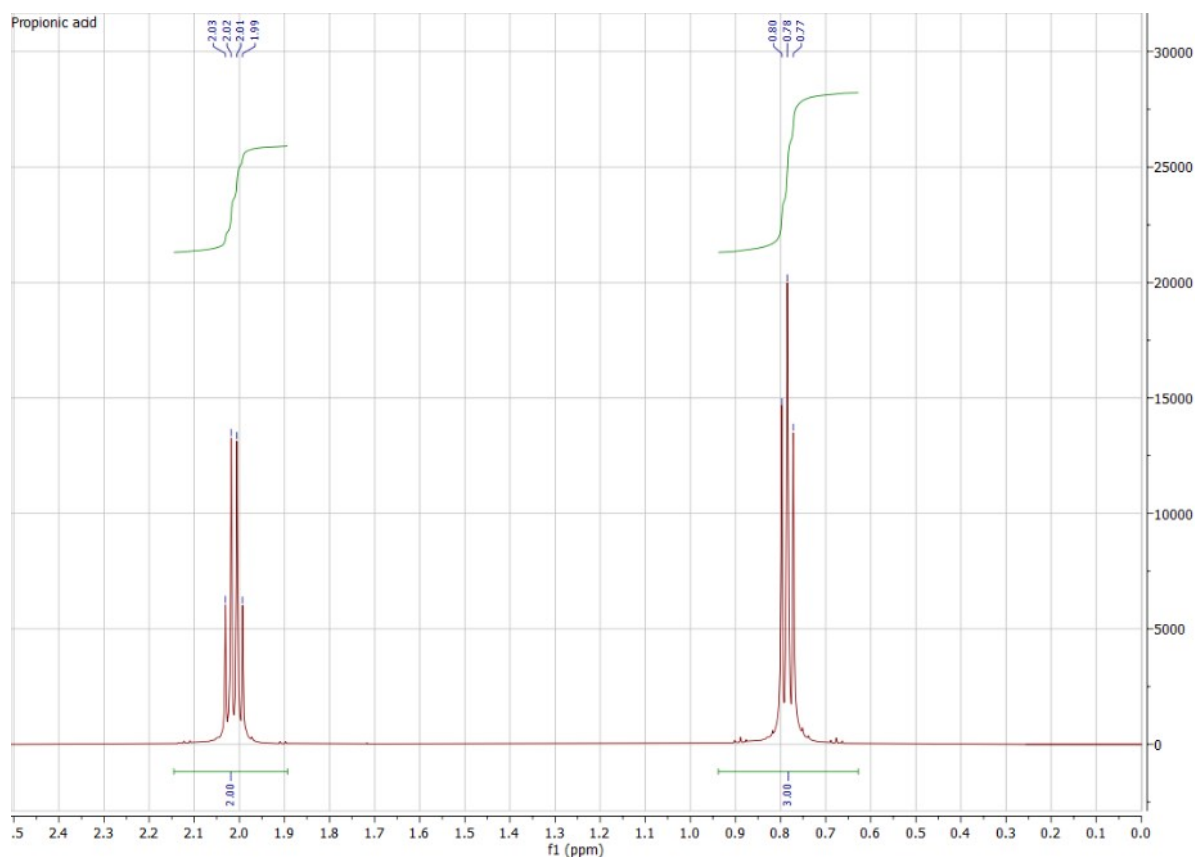
Figure S21 ^{1}H-NMR of propionic acid in NaOD/D$_2$O.
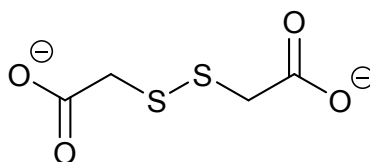
Figure S22 Dithioglycolate.

Following these results, we calculated the linker:modulator molar ratio with the hereafter presented calculations. In the calculations we used the term PA$^-$ (propionate, 2 protons) for the reaction products formed in the cross-coupling reaction and the term disulfide for residual dithioglycolate (4 protons). Since this is also formed from the modulator it must be included in the calculations for the molar ratio. We would like to note that at higher amounts of incorporated modulator the integral of the reaction product from the disulfide gets higher. Literature states that the oxidation of thiols to disulfide species with oxygen is catalyzed under basic conditions, which is why the MAc$^-$ modulator first reacts to the disulfide species, which can then undergo the C-C cross-coupling reaction.[3]

These results were cross-checked with the linker:modulator ratios determined by TGA (see Table 1). The results from NMR and TGA are in the same order of magnitude.

For the analysis of the modulator incorporation it is important to know the molar ratio (m_R) of the modulator MAc$^-$ to BDC^{2-}:

$$\frac{Modulator\ MAc^-}{BDC\ Linker^{2-}} m_R \qquad (1)$$

The integrals from the measured NMR spectrum give the relative number of equivalent active nuclei and the relative number of correlated species is then obtained by normalizing the integrals (Eq. 2)

$$m_R = \left(\frac{1H\ Integral\ Modulator}{N_{H\ Modulator}}\right) * \left(\frac{N_{H\ Linker}}{1H\ Integral\ Linker}\right) \qquad (2)$$

With $N_{HModulator}$ and $N_{HLinker}$ as the number of equivalent ^{1}H nuclei of Mac$^-$ (2 for CH$_2$) and BDC^{2-} (4 in C$_6$H$_4$) species, respectively. ^1H Integral Modulator and $1H$ Integral Linker$^-$ represent the numerical value of the ^{1}H NMR integrals. To simplify the calculation the $1H$ Integral Linker was set to 4 in accordance to literature, [4] thus:

$$\left(\frac{N_{HLinker}}{1H\ Integral\ Linker}\right) = \frac{4}{4} = 1$$
.

Eq. 2 then simplifies to:

$$m_R = \left(\frac{1H\ Integral\ MAc^-}{2}\right) * \left(\frac{4}{4}\right) \qquad (3)$$

We assign the singlet at 2.07-2.1 ppm to the -CH$_2$ group of mercaptoacetic acid and the quartet at 2.3 ppm to two molecules of propionic acid derived from the cross-coupling reaction of dithioglycolate with methanol. This integral must be added to the modulator contribution. The additional two small singlets at 3.1-3.2 ppm originate from unreacted dithioglycolate (Fig. S22) and are also visible in the ^{1}H-NMR spectrum of pure mercaptoacetic acid in NaOD/D$_2$O (Fig. S21). The two singlets also refer to four protons.

For the two protons of propionic acid, denoted as PA$^-$ N$_H$ is 2. For the two signals from dithioglycolate N$_H$ is also 4.The formula for the adjusted molar ratio of BDC^{2-}: MAc$^-$ is then given by:

$$\frac{Modulator}{Linker} m_R = \left[\left(\frac{1H\ Integral\ MAc^-}{2}\right) + \left(\frac{1H\ Integral\ Disulfide}{4}\right) + \left(\frac{1H\ Integral\ PA^-}{2}\right)\right] * \left(\frac{4}{4}\right) \qquad (4)$$

Table S3 Determination of incorporated modulator amount in UiO-66-MAc-x from ^{1}H-NMR.

UiO-66-MAc-	^{1}H Integral MAc$^-$	^{1}H Integral Disulfide	^{1}H Integral PA$^-$	BDC^{2-}: MAc$^-$ ^{1}H-NMR
10eq	0.12	0.34	0.30	1: 0.30
30eq	0.31	0.08	0.88	1: 0.62
50eq	1.25	0.59	-	1: 0.77
100eq	1.14	0.29	-	1: 0.64

The NMR results show slight deviations from the TGA weight loss analysis (Table 1). These differences can be ascribed to slight inaccuracies in determining the weight loss steps in the TGA analysis or by an incomplete digestion of the MOF samples in the NMR experiments.

S3.3 Elemental analysis (CHNS)

Table S4 Elemental analysis (CHNS) of UiO-66-MAc-10eq, -30eq, -50eq and -100eq.

UiO-66-MAc	C [wt%]	H [wt%]	N [wt%][a]	S [wt%]
10eq	29.33	2.34	–	3.70
30eq	28.90	2.60	1.32	4.84
50eq	26.70	2.80	-	6.77
100eq	26.04	2.50	-	4.60

[a] The nitrogen in UiO-66-MAc-30eq is due to the presence of residual solvent (*N,N*-dimethylformamide, DMF).

Table S5 Sum formulae of UiO-66-MAc with comparison of calculated and found ratios BDC^{2-}: MAc^-, Zr: S and S content based on NMR - and TGA-derived sum formula.

| UiO-66-MAc	Exp. ratio BDC^{2-}: MAc^- average [a]	Sum formula from BDC^{2-}: MAc^- average [a] based on NMR, TGA weight loss and defect calc. [a,b]	Calc. ratio Zr: S (based on sum formula)	Exp. ratio Zr: S [c] from SEM-EDX	Theor. sulfur content [wt%] (based on sum formula	Exp. S from CHNS [d] [wt%]
10eq	1: 0.31	$Zr_6O_4(OH)_4(BDC)_{4.58}(MAc)_{1.42}$	1 :0.24	1: 0.28	2.92	3.70
30eq	1: 0.56	$Zr_6O_4(OH)_4(BDC)_{3.85}(MAc)_{2.15}$	1: 0.36	1: 0.49	4.57	4.84
50eq	1: 0.80	$Zr_6O_4(OH)_4(BDC)_{3.33}(MAc)_{2.67}$	1: 0.45	1: 0.41	5.83	6.77
100eq	1: 0.57	$[(Zr_6O_4(OH)_4)_2(OH)_6](BDC)_{5.73}(MAc)_{3.27}$	1: 0.27	1: 0.27	4.03	4.60

[a] See Table 1. [b] Sum formula calculated from the average linker to modulator ratios under the assumption that one BDC^{2-} linker in ideal **fcu**-UiO-66 with $[Zr_6O_4(OH)_4(BDC)_6]$ and in ideal **hcp**-UiO-66 with $[(Zr_6O_4(OH)_4)_2(OH)_6(BDC)_9]$ is replaced by two MAc^- molecules. [c] Table S2, ESI. [d] Table S4, ESI†.

S4 Thermogravimetric studies

S4.1 Interpretation of the weight loss in the TGA curves

Up to approximately 150 °C residual solvent is removed from the pores. In the next step from 150 up to 390 °C the removal of the monocarboxylate modulator and the dehydroxylation of the SBU occurs. Literature states that these two processes happen at similar temperature zones and are usually difficult to be seperated.[4] During the dihydroxylation UiO-66 loses two equivalents of water from the zirconium-bridging hydroxyl groups and changes the SBU from $\{Zr_6(OH)_4O_4\}$ to the dehydroxylated form $\{Zr_6O_6\}$.

At ~400 °C the BDC linker decomposes up to approximately 550 °C. The remaining residue is ZrO_2. For the hcp structured UiO-66 Ermer *et al.* stated that at 560 °C the compound formed a mixed phase of C/ZrO_2 which is expected to decompose at higher temperatures.[5] In our case the decomposition was still not finished at 1000 °C (no final plateau). TGA curves for the modulated MOFs are presented in Fig. S23
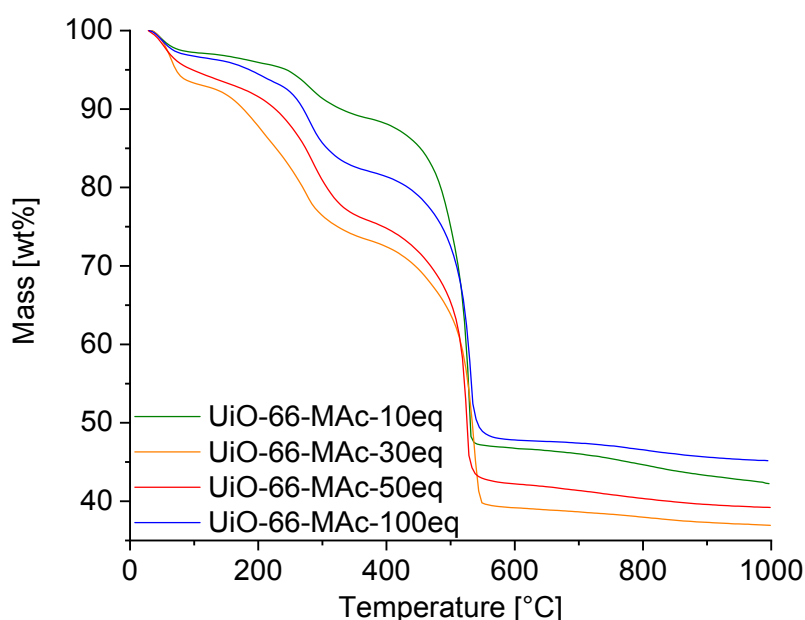
Figure S23 TGA curves of MAc⁻ modulated UiO-66 type MOFs.

To determine the ratios of BDC^{2-} to MAc⁻ directly from the TGA curves we analyzed weight loss steps of the curves. The weight loss attributed to the decomposition of the organic linker was set to a value of 1 and the ratio BDC^{2-}: MAc⁻ was calculated. Weight loss steps are shown in Fig. S24- S27.
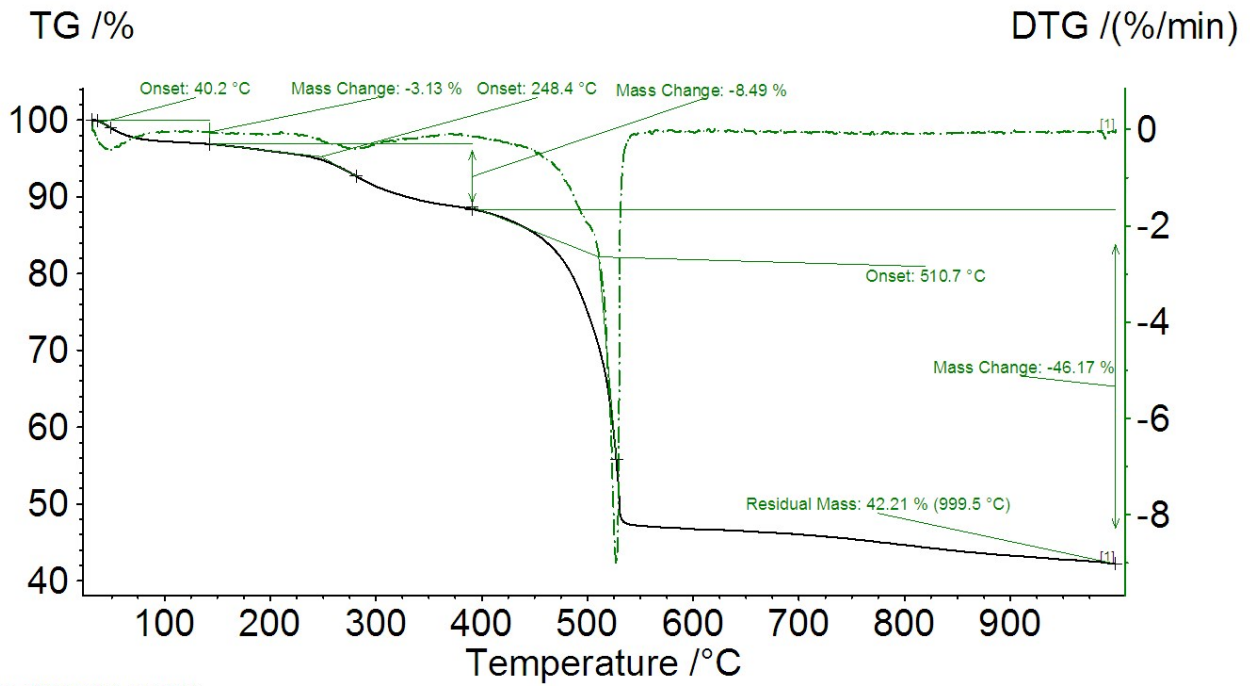
Figure S24 TGA curve with weight loss steps for UiO-66-MAc-10eq.
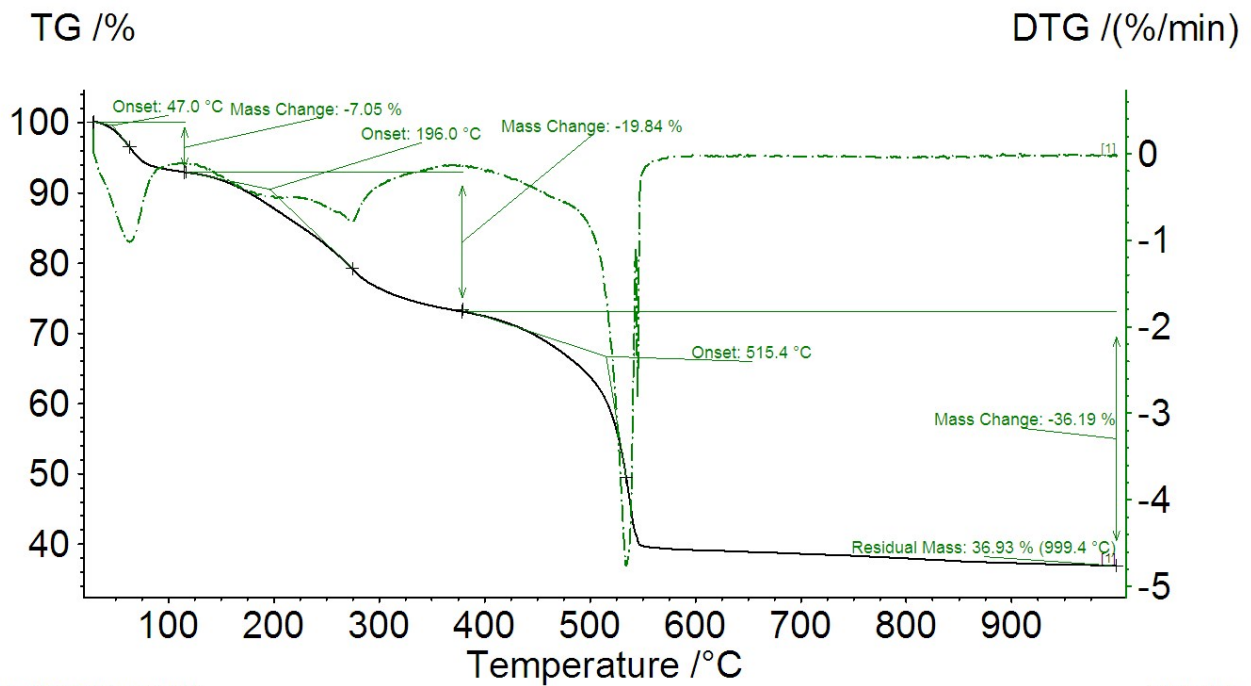
Figure S25 TGA curve with weight loss steps for UiO-66-MAc-30eq.
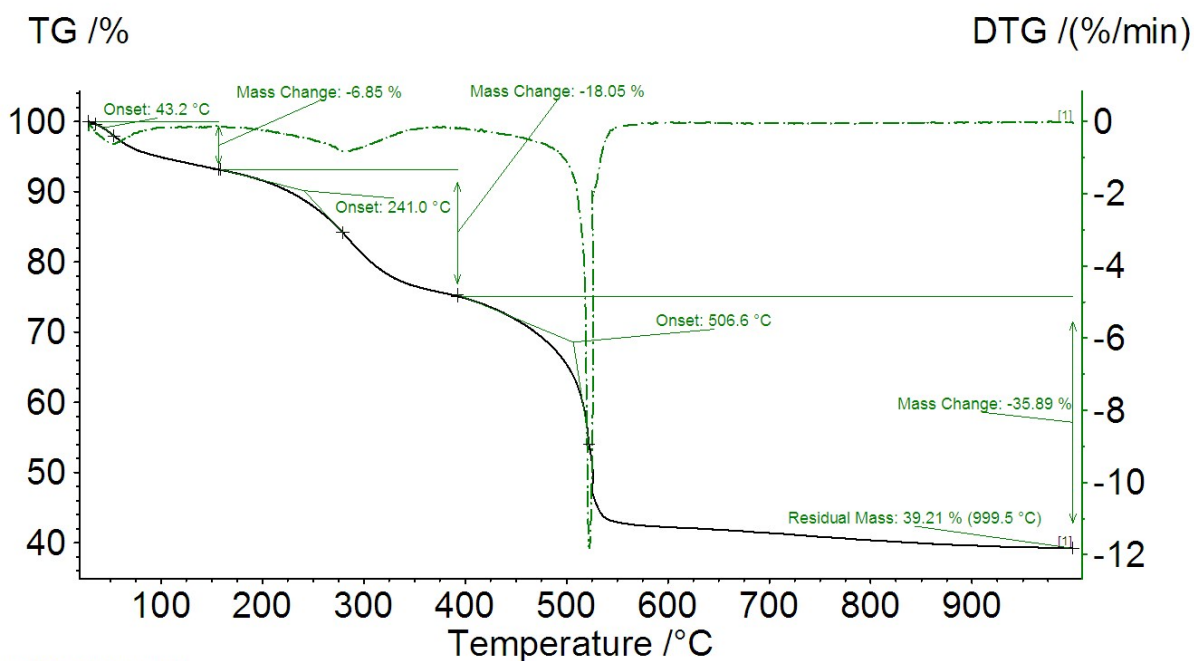
Figure S26 TGA curve with weight loss steps for UiO-66-MAc-50eq.
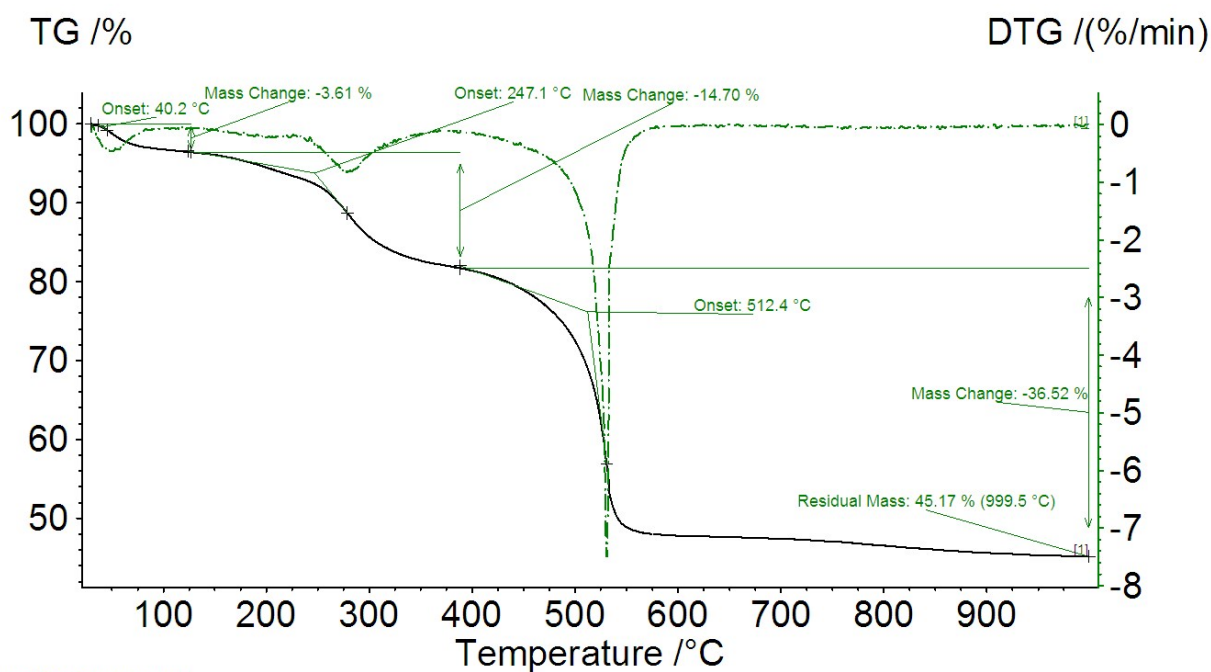
Figure S27 TGA curve with weight loss steps for UiO-66-MAc-100eq.

The weight loss in % and the calculated BDC^{2-}: MAc^- ratio from the TGA curves is presented in Table S6.

Table S6 Weight loss of BDC^{2-} and MAc^- and calculated linker: modulator ratio for UiO-66-MAc-Xeq.

UiO-66-MAc	Weight loss BDC^{2-} [%]	Weight loss MAc$^-$ [%]	Ratio BDC^{2-}: MAc$^-$
10eq	46.17	11.62	1: 0.29
30eq	36.19	19.84	1: 0.55
50eq	35.89	24.90	1: 0.85
100eq	36.52	18.31	1: 0.50

S4.2 Quantification of linker defects from TGA curves and calculated sum formulae

Linker defects are quantified with the method introduced by Shearer et al.[4] In order to use this method some assumptions must be made. The remaining residue after the TGA analysis must be zirconium(IV) oxide (ZrO_2). Therefore, all the solvent, the modulator and the organic linker were completely decomposed during the TGA. The reaction scheme for decomposition of ideal (dehydroxylated) UiO-66 is:

$$Zr_6O_6(BDC)_6 \text{ (s) } + 45\ O_2 \text{ (g)} \longrightarrow 6\ ZrO_2 \text{ (s) } + 48\ CO_2 \text{ (g) } + 12\ H_2O \text{ (g)}$$
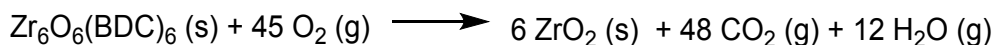
One SBU of UiO-66 will yield six equivalents ZrO_2. The molar mass of $Zr_6O_6(BDC)_6$ is 1628.03 g/mol.

Six mol of ZrO_2 (molar weight: 123.22 g/mol) have a combined molar mass of 739.34 g/mol. Under the assumption that all residual mass on the TGA experiments consists of ZrO_2 the residual mass is normalized to 100% in this method. Afterwards it is possible to calculate a theoretical plateau ($W_{Theo.Plat}$) in the TGA for empty, solvent-free dehydroxylated UiO-66. Therefore, the molar mass of one SBU **(= M_{Comp})** is divided by the molar mass of six mol ZrO_2 **(= M_{6*ZrO2})** and multiplicated with the to 100% normalized residual weight **(= W_{end})**.

$$W_{Thero.\,Plat.} = \frac{M_{Comp}}{M_{6 \times Zr = 2}} \times W_{end}$$

(5)

With the aforementioned molar weights $W_{Theo.Plat.}$ is: $\left(1628.03\frac{g}{mol} \times 739.34\frac{g}{mol}\right) \times 100\ \% = 220.20\ \%$

The weight contribution per BDC^{2-} unit to the total weight **(Wt.PL$_{Theo.}$)** is calculated next. **NL_{ideal}** is the number of linker molecules in an ideal UiO-66 **(NL_{ideal} = 6)**.

$$Wt.PL_{Theo} = \frac{(W_{Theo.\,Plat.} - W_{end})}{NL_{ideal}}$$

(6)

$$Wt.PL_{Theo.} = \frac{220.20\ \% - 100\ \%}{6} = 20.03\ \%$$

The number of linker molecules in a Zr_6-SBU with defects can be calculated as:

$$NL_{Exp} = (6 - x) = \frac{W_{Exp.\,Plat.} - W_{end}}{Wt.PL_{Theo}}$$

(7)

$W_{Exp.Plat}$ can be deduced from the experimental TGA curve.

Afterwards the number of defects per Zr_6-SBU is calculated:

$$x = 6 - NL_{exp} = \left(\frac{(W_{Exp.\,Plat.} - W_{end})}{Wt.PL_{Theo.}}\right)$$

(8)

Now the chemical formula and the molar mass can be calculated:

$$M_W = Zr_6O_{6+x}(BDC)_{6-x}$$

The residual mass of ZrO$_2$, was normalized to 100% to calculate linker defects, the chemical formula, and the molecular weight of the defect UiO-66-MAc.
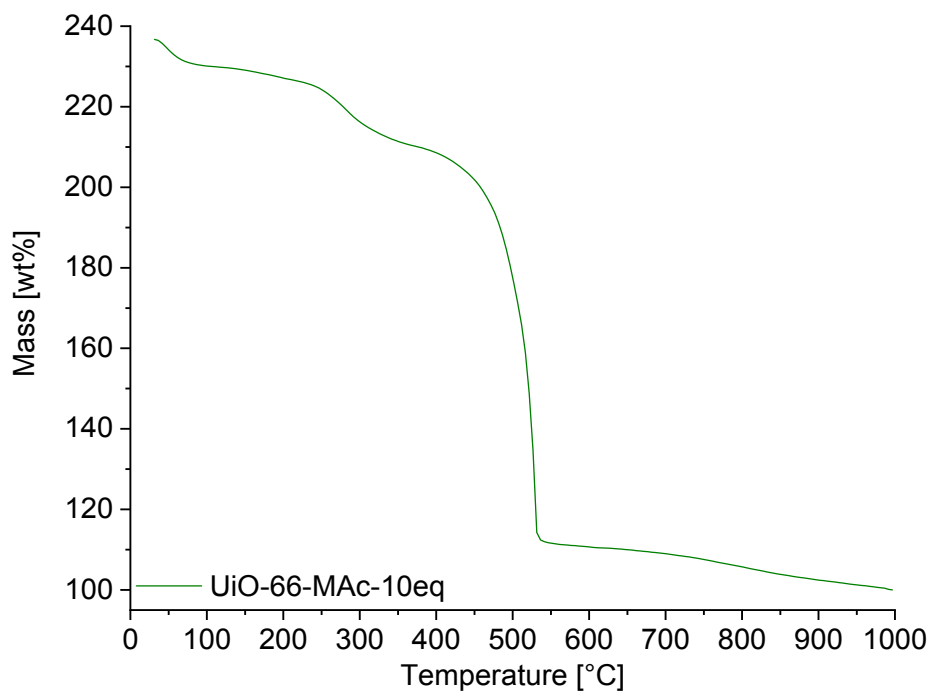
Figure S28 TGA curve of UiO-66-MAc-10eq (normalized to 100 % residual mass).
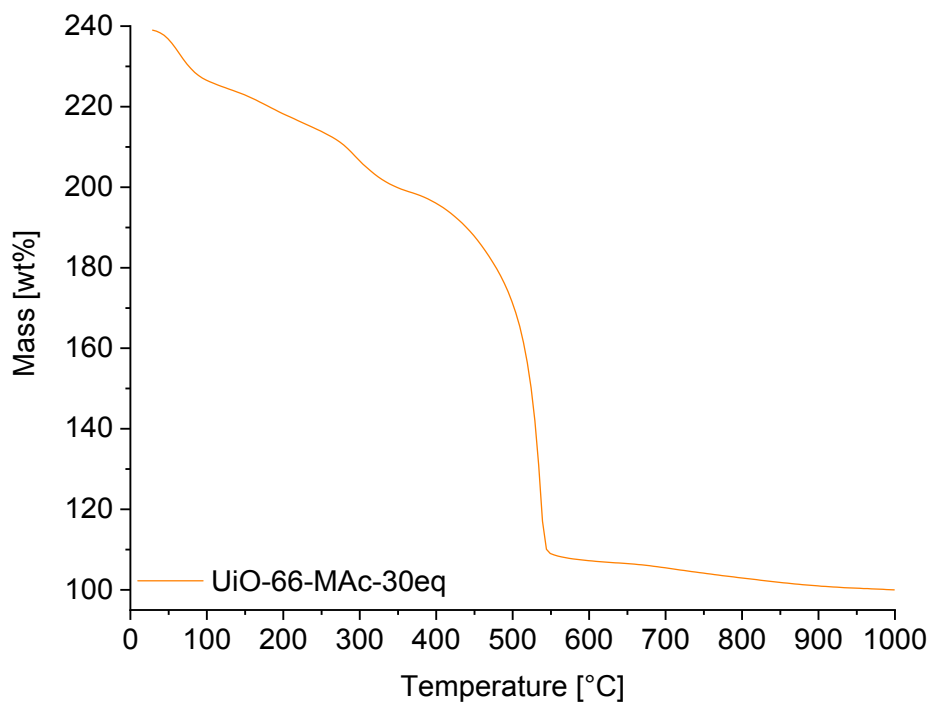
Figure S29 TGA curve of UiO-66-MAc-30eq (normalized to 100 % residual mass).
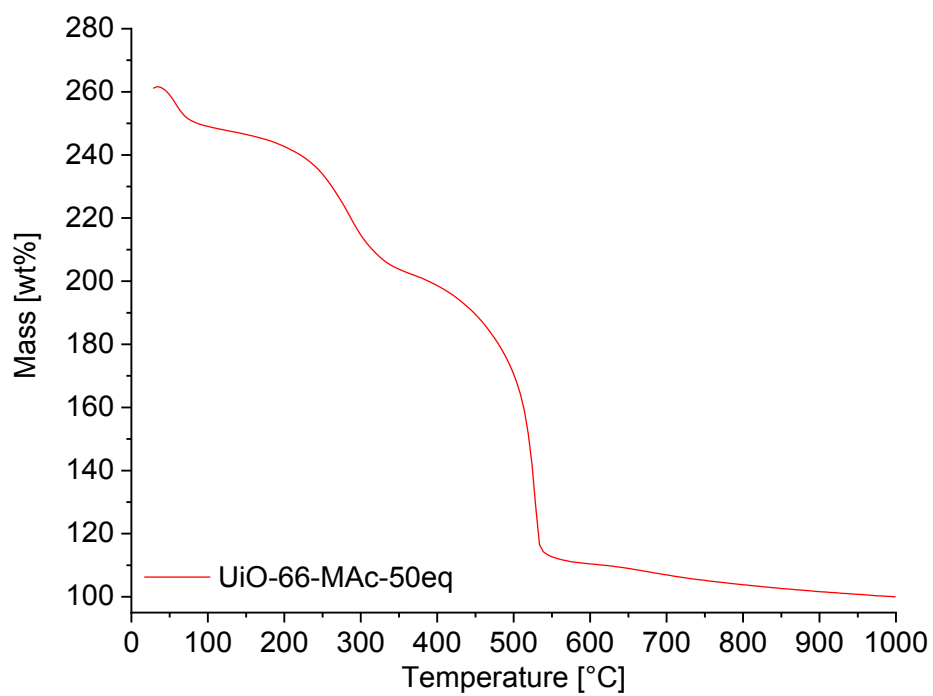
Figure S30 TGA curve of UiO-66-MAc-50eq (normalized to 100 % residual mass).
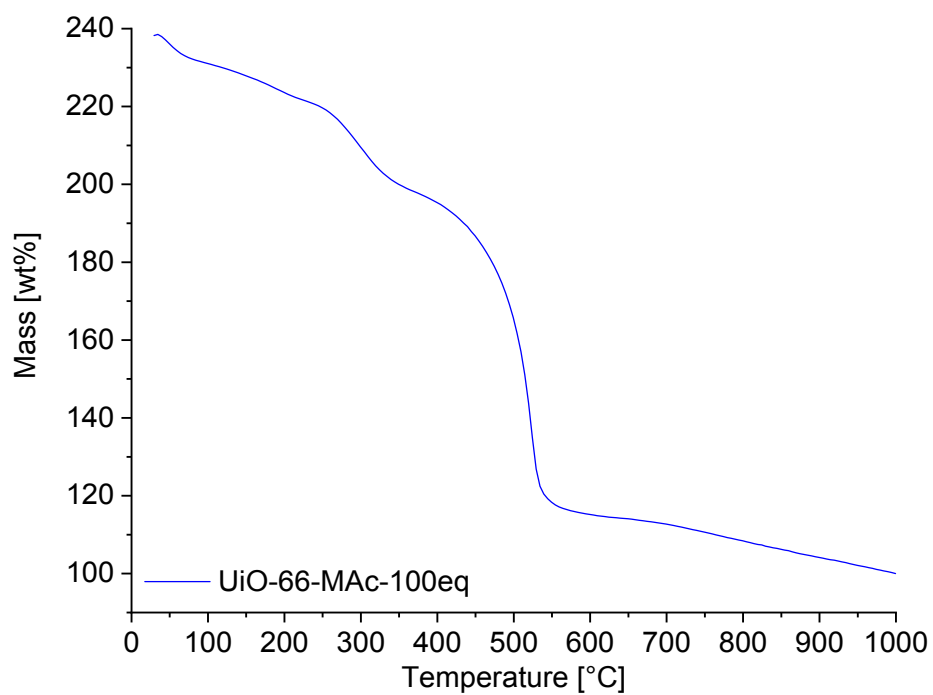
Figure S31 TGA curve of UiO-66-MAc-100eq (normalized to 100 % residual mass).

Table S7 Linker defects and calculated sum formula and molar weights for UiO-66-MAc-10eq, UiO-66-MAc-30eq and UiO-66-MAc-50eq. Plateau [wt%] is used for **W$_{Exp.Plat}$**.

UiO-66-MAc	Plateau [°C]	Plateau [wt%]	x	BDC	Chem. formula from linker defects	Mw [g/mol]
10eq	420	203	0.9	5.1	$Zr_6O_{6.9}(BDC)_{5.1}$	1494.73
30eq	399	196	1.2	4.8	$Zr_6O_{7.2}(BDC)_{4.8}$	1450.29
50eq	460	187	1.7	4.3	$Zr_6O_{7.7}(BDC)_{4.3}$	1658.79

Under the assumption that each missing BDC^{2-} linker is replaced by two MAc$^-$ ligands we can give the general chemical formula for UiO-66-MAc as $[Zr_6O_6(BDC)_{6-x}(MAc)_{2x}]$.

The average linker:modulator ratio (Table 1) derived from the molar BDC^{2-}:MAc$^-$ ratio from NMR and direct TGA analysis, together with the defect chemical formula from TGA analysis, were the basis for a sum formula under the assumption, that one BDC^{2-} linker in ideal **fcu**-UiO-66 with $[Zr_6O_4(OH)_4(BDC)_6]$ and in ideal **hcp**-UiO-66 with $[(Zr_6O_4(OH)_4)_2(OH)_6(BDC)_9]$ is replaced by two MAc$^-$ molecules (Table S7).

S5 FT-IR and FT-Raman spectroscopy
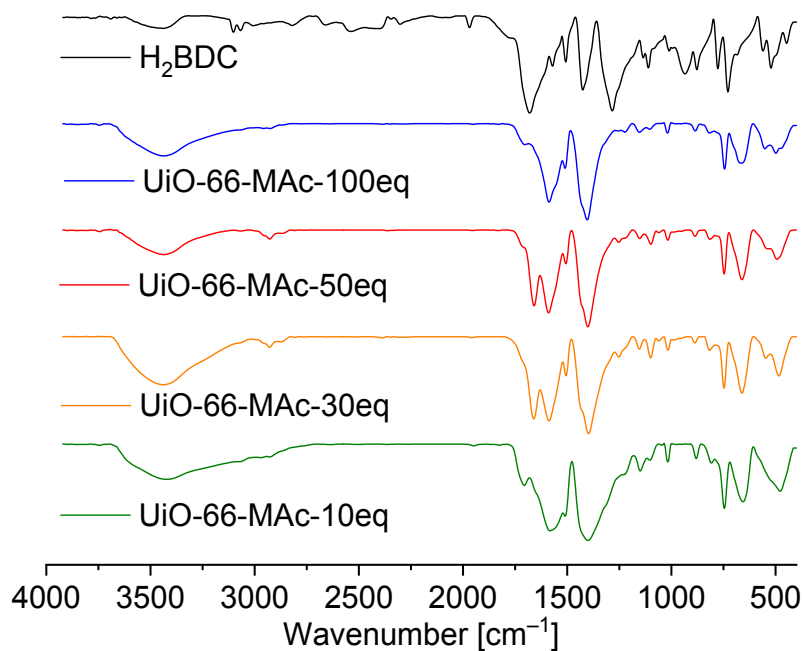
Figure S32 Comparison of the FT-IR spectra of the organic linker H_2BDC and UiO-66-MAc-10eq, -30eq, -50eq and -100eq.

The FT-IR spectra of the UiO-66-MAc MOFs present strong absorption bands at 1590 and 1400 cm^{-1}, which can be ascribed to the asymmetric and symmetric stretching vibrations from $-CO_2$ of the carboxylic linker (Figure S32, ESI†). The disappearance of the -OH vibration of the free carboxylic acid at 1280 cm^{-1} marks the successful deprotonation and indicates the incorporation of the organic linker H_2BDC as BDC^{2-}. All FT-IR spectra show no visible vibrations assignable to the MAc^- modulator. This is due to the small amounts of incorporated modulator and the weak vibration intensities for the thiol group in IR-spectroscopy.
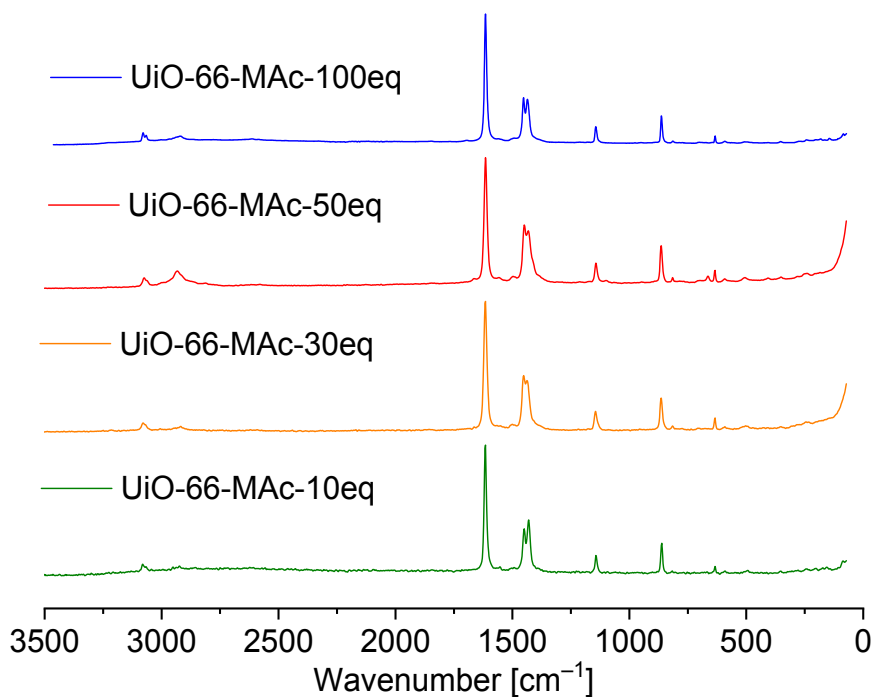
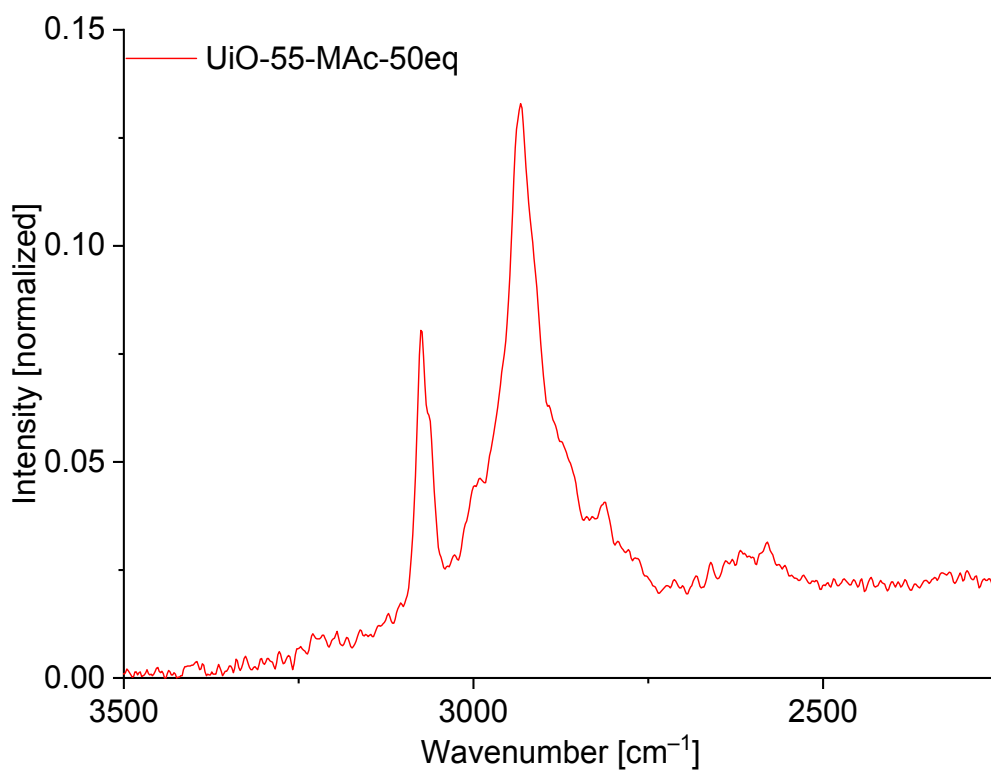**Figure S33** Comparison of the FT-Raman spectra of the organic linker H_2BDC and UiO-66-MAc-10eq, -30eq, -50eq and -100eq.

The Raman spectra (Figure S33, ESI†) show the disappearance of the carboxylic acid vibration at 1290 cm^{-1} and a strong double signal at 1450 and 1432 cm^{-1} of the BDC^{2-} carboxylate group. The vibration at 1615 cm^{-1} is caused by C=C stretching vibrations in the aromatic BDC^{2-} linker. For the 50eq and 100eq modulated UiOs, the signals at 2580 cm^{-1} can be assigned to -SH vibrations (see Fig. S34 and S35, ESI†) and were reproducibly visible after enhancing the laser power up to 700 mW and using prolonged measurement times. The relatively small amount of -SH groups on the surface of the MOF only results in very small Raman signals, since some thiol bonds were oxidized to dithiol groups and the major amount of -SH groups is expected to be inside the material, leaving only a small number of measurable thiol groups that were excitable by the laser.

Figure S34 Section of the FT-Raman spectra UiO-66-MAc-50eq (2200-3500 cm^{-1}).
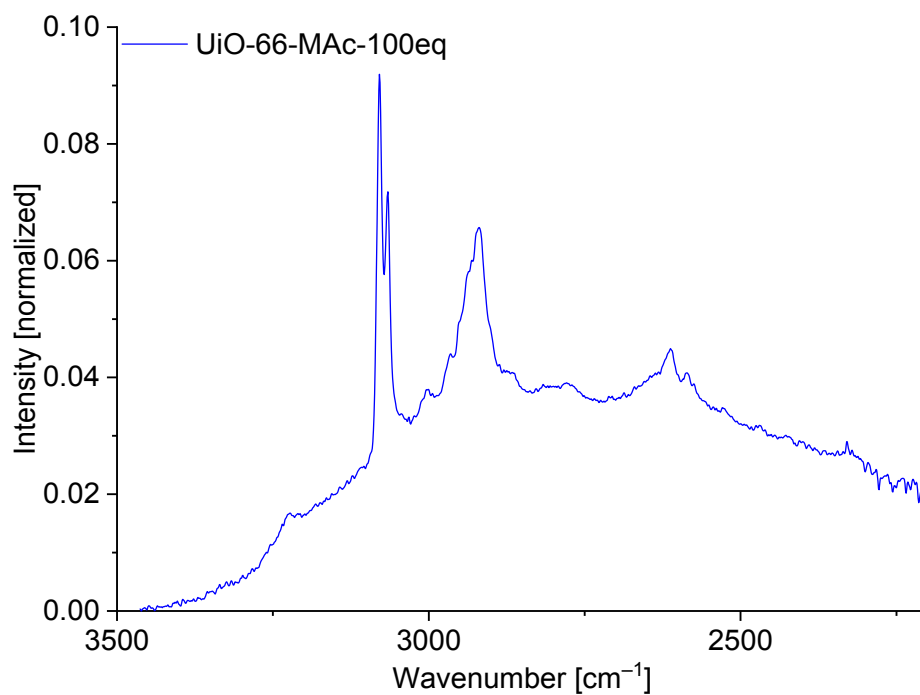
Figure S35 Section of the FT-Raman spectra UiO-66-MAc-100eq (2200-3500 cm^{-1}).

Figure S36 Ar sorption isotherm of UiO-66-MAc-50eq at 87 K. Filled symbols: adsorption; empty symbols: desorption.
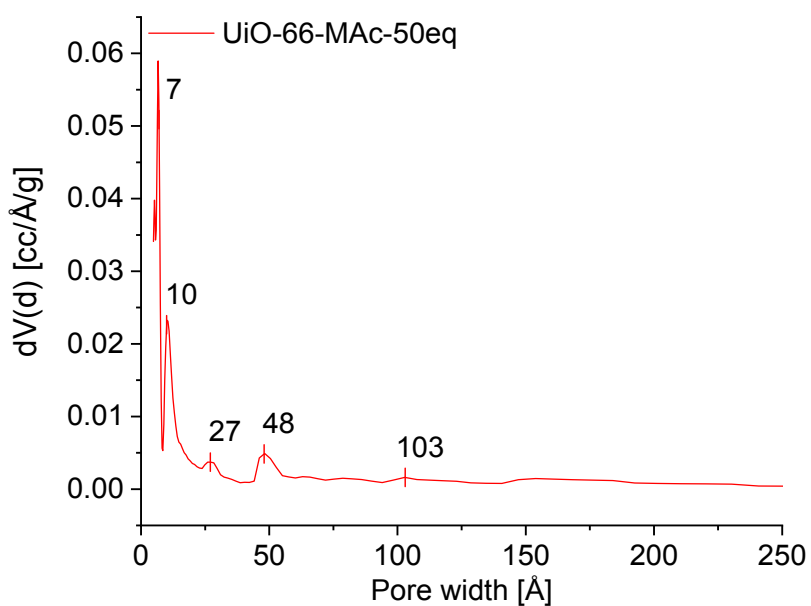
Figure S37 Pore size distribution of UiO-66-MAc-50eq calculated with QSDFT from Argon physisorption at 87 K (using the "Ar at 87 K Carbon QSDFT, slit pore, QSDFT equilibrium" model).
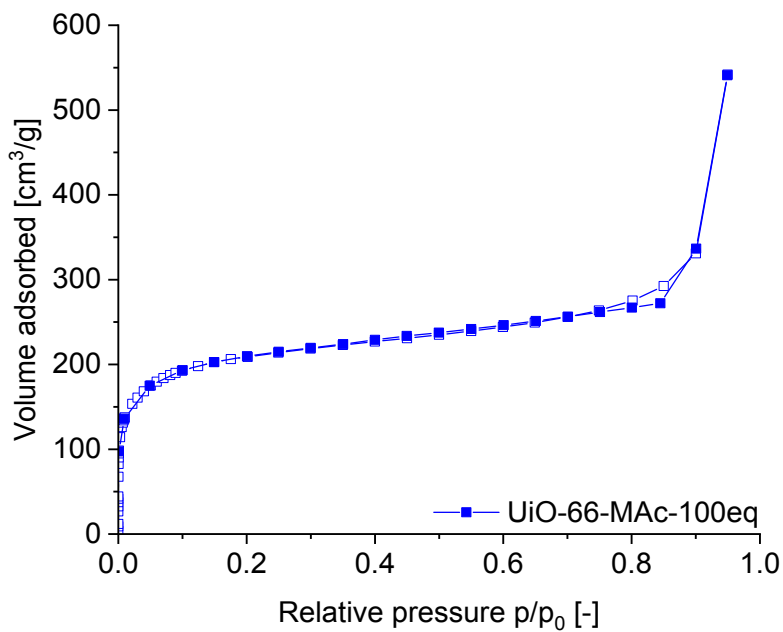
Figure S38 Ar sorption isotherm of UiO-66-MAc-100eq at 87 K. Filled symbols: adsorption; empty symbols: desorption.
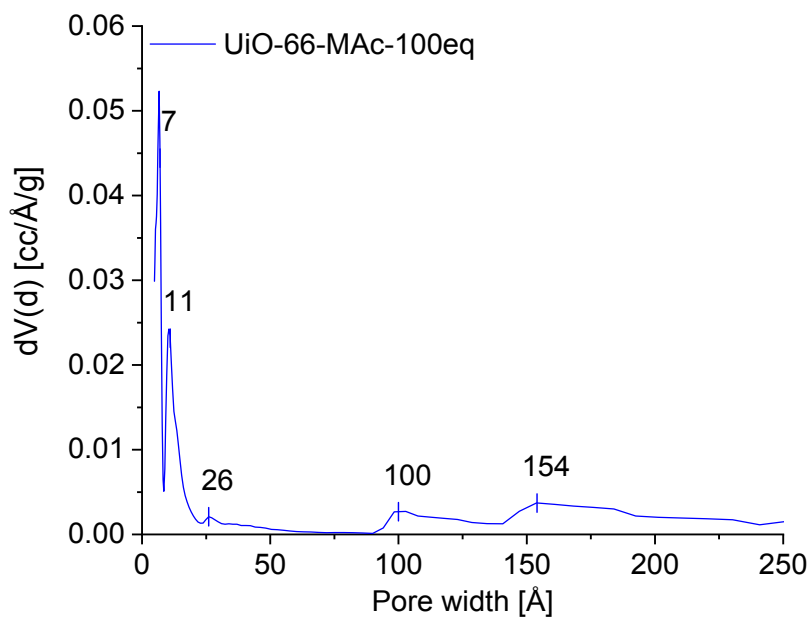
Figure S39 Pore size distribution of UiO-66-MAc-100eq calculated with QSDFT from Argon physisorption at 87 K (using the "Ar at 87 K Carbon QSDFT, slit pore, QSDFT equilibrium" model).
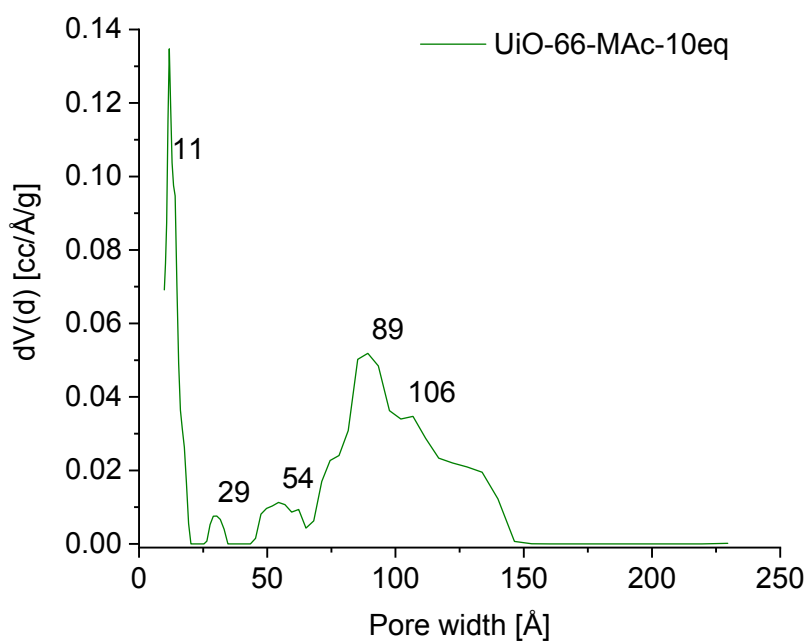
Figure S40 Pore size distribution of UiO-66-MAc-10eq calculated with DFT calculation from nitrogen physisorption at 77 K.
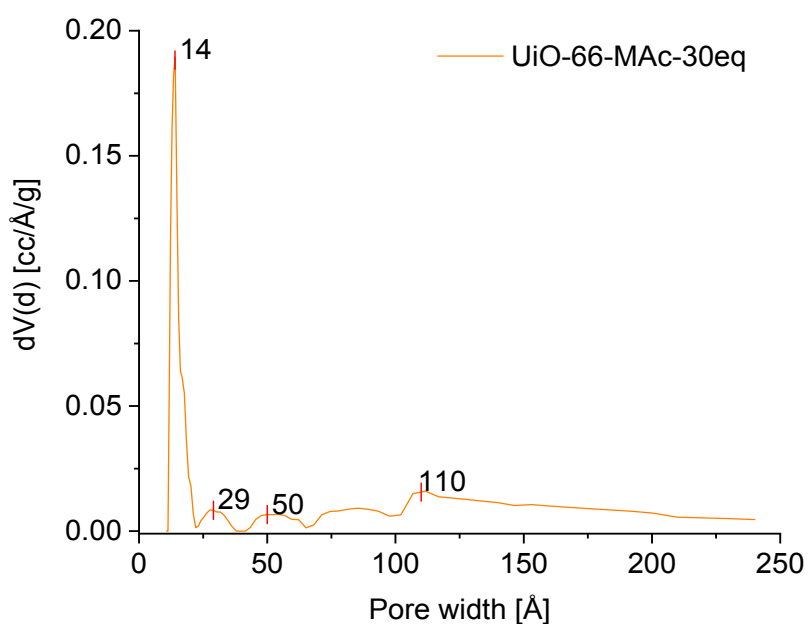
Figure S41 Pore size distribution of UiO-66-MAc-30eq calculated with DFT calculation from nitrogen physisorption at 77 K.

Pore size distributions for UiO-66-MAc-10eq and -30eq were determined by nitrogen physisorption. Because of a higher inaccuracy of nitrogen against argon in determining pore sizes and limitations in the sensor of the used device, it was not possible to measure pore sizes under 10 Å with nitrogen at 77 K. However, the measured pore sizes for UiO-66-MAc-10eq and UiO-66-MAc-30eq are in the same order of magnitude as the pore sizes determined by argon physisorption.

S7 Structural information of hcp UiO-66-MAc-100eq and fcu UiO-66.

The structure of the **hcp** phase of UiO-66 can be described in two ways. In **hcp** UiO-66 two of the typical Zr-clusters $[Zr_6O_4(OH)_4]$ in UiO-66 are joint through the bridging action of six μ-OH groups. The SBU can then be described with the chemical formula $[Zr_{12}O_8(OH)_{14}]$ which is connected by 18 terephthalate linkers to neighboring SBUs (Fig. S42).[5]
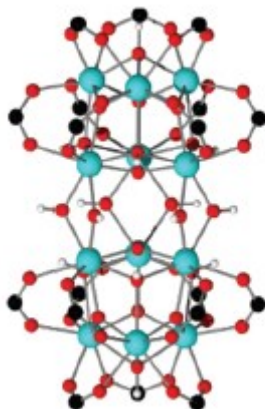
Figure S42 Zr_{12} cluster of **hcp** UiO-66. (Figure adapted from reference 5.)

The connected clusters form wave-like chains along the a- and b-axis with channels along the c-axis (Figure S43).[5]
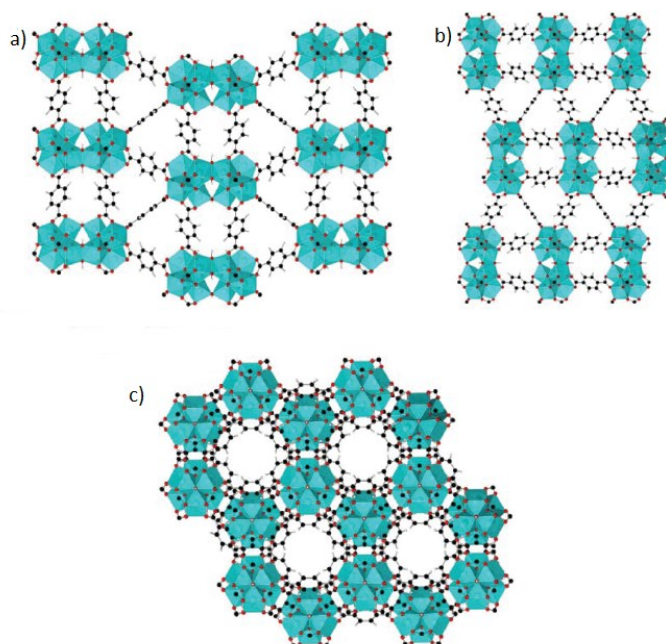
Figure S43 Structure of **hcp** UiO-66 along a-axis (a), b-axis (b) and channels along the c-axis (c). Zr clusters are shown as cyan colored polyhedral, connected by linker molecules. (Figure adapted from reference 5.)

In most synthesis routes UiO-66 is formed with a face-centered cubic (**fcu**) structure and the sum formula $Zr_6O_4(OH)_4BDC_6$. The secondary building unit $\{Zr_6O_4(OH)_4(CO_2)_{12}\}$ is an octahedral cluster of six vertex-sharing ZrO_8 square-antiprism. In the inner core of the SBU $\{Zr_6O_4(OH)_4\}$ the triangular faces of the Zr_6-octahedron are alternatively capped by μ_3-OH and μ_3-O groups. The resulting SBU is 12-coordinated by the organic linker

which is equal to the metal atoms in close-packed metal structures and forms one of the highest known coordination numbers for the SBU of a MOF.

This connection of neighboring SBUs results in tetrahedral and octahedral cages which combine to the face-centered cubic packing (Fig. S44) of UiO-66.[6,7]
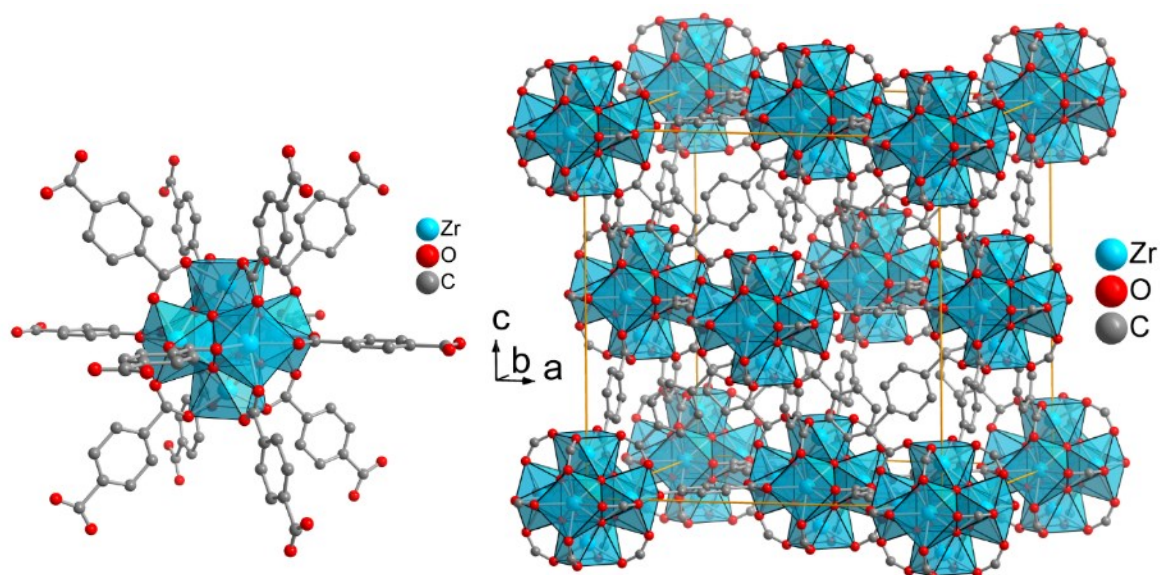
Figure S44 Structure of zirconium terephthalate UiO-66, 3D-[$Zr_6O_4(OH)_4(BDC)_6$]. On the left side the SBU with the 12 terephthalate linker molecules. On the right side the packaging along a-,b- and c-axis forming the **fcu** structure is shown. UiO-66 structure is drawn from the deposited cif files under CCDC 837796.[8] (Figure adapted from reference 7.)

S8 Stability tests of UiO-66-MAc-50eq and UiO-66-MAc-100eq

Figure S45 PXRD patterns of UiO-66-MAc-50eq after 24 h in water (pH 7) or buffer with pH 4 and pH 10.

Figure S46 PXRD patterns of UiO-66-MAc-100eq after 24 h in water (pH 7) or buffer with pH 4 and pH 10.

S9 Adsorption models

S9.1 Langmuir model[9]

Langmuir adsorption equation is shown in formula (9):

$$q_e = \frac{k_L q_{max} c_e}{1 + k_L c_e} \qquad (9)$$

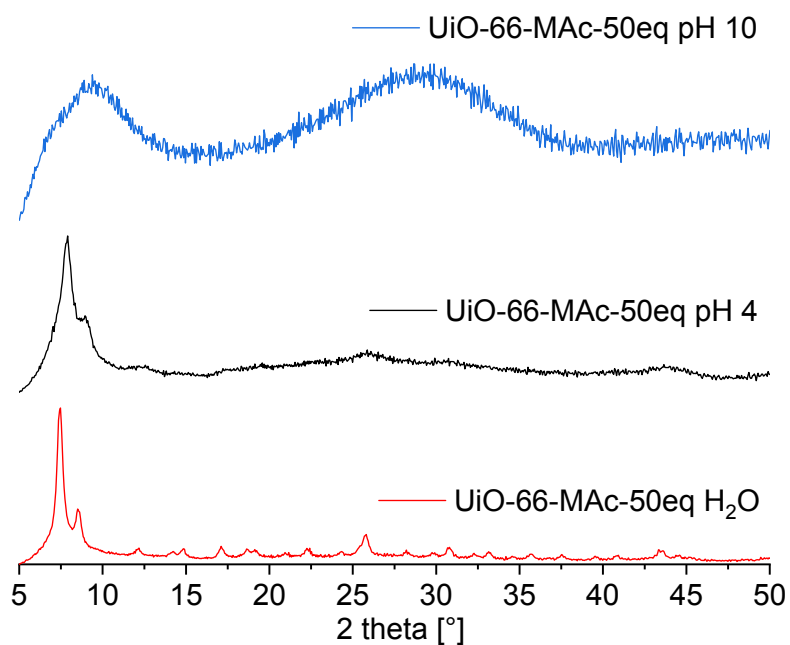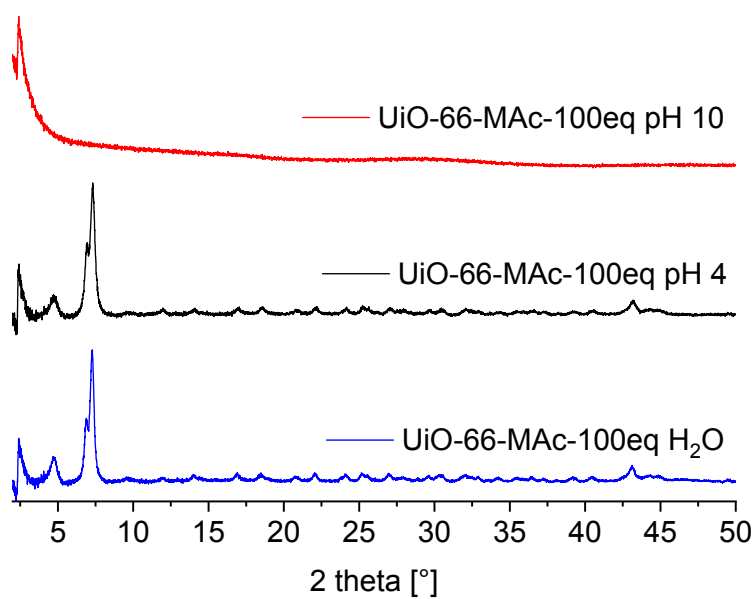Where c_e [mg L^{-1}] is the equilibrium concentration of silver(I) ions in the solution, q_e [mg g^{-1}] is the adsorbed amount of silver(I) at equilibrium and k_L is the Langmuir constant [L mg^{-1}] and is therefore related to affinity of the binding sites and the adsorption energy. Finally, q_{max} is the maximum capacity of adsorbed silver(I) [mg g^{-1}].

To check the usage of the model the linearized version was used. If the experimental fit shows a high correlation factor between c_e/q_e and c_e it can be assumed that the Langmuir adsorption model displays the adsorption of silver(I) to our modified MOF. The linearized formula is given in formula (10)

$$\frac{C_e}{q_e} = \frac{1}{q_{max} k_L} + \frac{C_e}{q_{max}} \qquad (10)$$

S9.2 Freundlich model[9]

The equation for the Freundlich adsorption model is shown in Formula (11)

$$q_e = k_F c_e^{(n)} \qquad (11)$$

The Freundlich constant k_F [mg^{1-n} L^n g^{-1}] is related to the adsorption capacity of silver(I) and n is used as a label for the adsorption intensity. In addition, the value of n reflects the isotherm type, whereas n = 0 indicates an unwanted irreversible adsorption, favorable values are 0<n<1. For values greater than 1 there is also an unfavorable shape of the adsorption.

As for the Langmuir model, a linearized formula[10] (12) is used here to fit the experimental data and to compare the linear regression of both models.

$$log(q_e) = log(k_F) + \frac{1}{n} log(c_e) \qquad (12)$$

For the linearization we fitted log (q_e) against log (c_e) and analyzed the linear regression.

S10 Kinetic models

S10.1 Linear pseudo second order kinetic model[11]

$$\frac{t}{q_t} = \frac{t}{q_e} + \frac{1}{k_2 q_e^2} \qquad (13)$$

With t is time [min], q_t [mg g⁻¹] is the amount adsorbed at time t and q_e [mg g⁻¹] is the adsorbed amount at equilibrium. k_2 [g mg⁻¹ min⁻¹] is the rate constant.

$$q_t = \frac{C_0 - C_t}{m_{MOF}} \qquad (14)$$

c_o is the starting concentration of silver(I) and c_t the silver(I) concentration at time t.

S10.2 Linear pseudo first order kinetic model[12]

$$ln(q_e - q_t) = ln\,(q_e) - k_1 t \qquad (15)$$

With t is time [min], q_t [mg g⁻¹] is the amount adsorbed at any time and q_e [mg g⁻¹] is the adsorbed amount at equilibrium. k_1 [g mg⁻¹ min⁻¹] is the rate constant.

S11 Freundlich adsorption model of UiO-66-MAc-50eq and UiO-66-MAc-100eq and kinetic studies for UiO-66-MAc-100eq

a)   b)
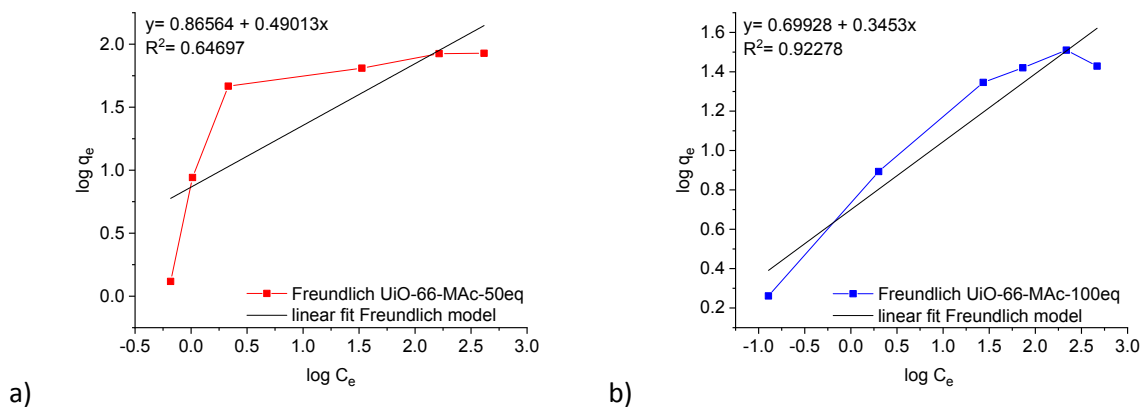
Fig. S47 Fitted equilibrium data by linearized Freundlich adsorption model for a) UiO-66-MAc-50eq and b) UiO-66-MAc-100eq.
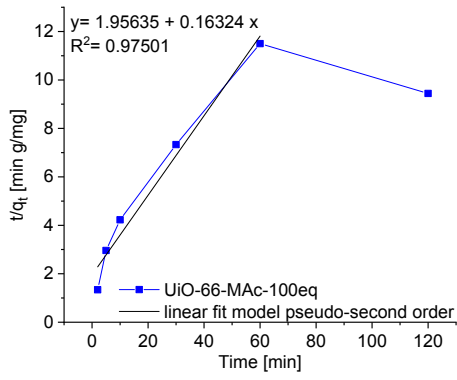
a)
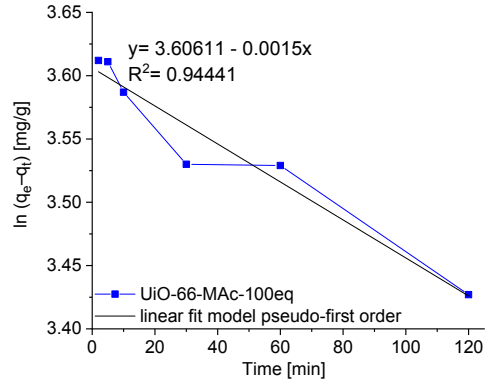
b)

Fig. S48 a) Time dependent removal of Ag(I) by UiO-66-MAc-100eq b) linear fit kinetic pseudo second order c) linear fit kinetic pseudo first order.

S12 Removal of Ag(I)-ions from aqueous solution with UiO-66-MAc-30eq

The removal of silver(I) ions from aqueous solution was additionally tested with UiO-66-MAc-30eq (Fig.S4 9). The MOF showed a maximum uptake of 53 mg/g at a concentration of 443 mg/L. UiO-66-MAc-50eq, which is also a **fcu** type UiO-MOF, showed a maximum uptake of 84 mg/g at a concentration of 164 mg/L. At this concentration UiO-66-MAc-30eq showed an uptake of 47 mg/g. The result is consistent with the higher sulfur content of UiO-66-Mac-50eq (6.77 wt%) compared to UiO-66-Mac-30eq (4.84 wt%). UiO-66-MAc-30eq showed a slightly higher sulfur content than **hcp** UiO-66-MAc-100eq (see Section S3, ESI†). UiO-66-MAc-100eq showed a maximum uptake of 32 mg/g at a concentration of 216 mg/L. At the same concentration UiO-66-MAc-30eq showed an Ag(I) uptake of 48 mg/g.

The results indicate a correlation of maximum Ag(I) uptake to sulfur content consistent with chemisorption following the Langmuir adsorption model.
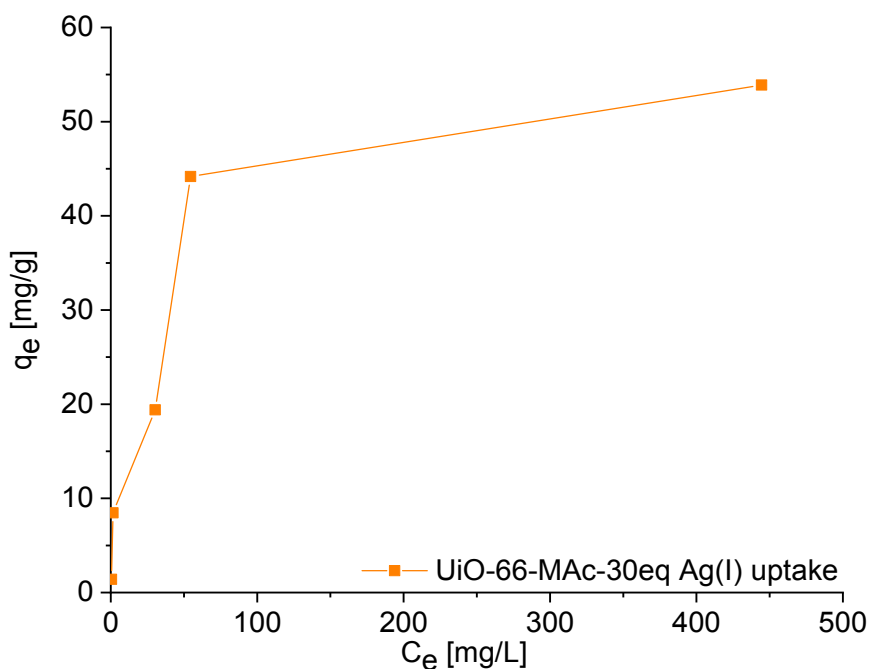
Figure S49 Isotherm of the Ag(I) removal with UiO-66-MAc-30eq.

S13 Analytical data of UiO-66-MAc-50eq and UiO-66-MAc-100eq after Ag(I) uptake and removal

S13.1.1 PXRD pattern and N$_2$-sorption experiments (77K) of UiO-66-MAc-50eq and -100eq after Ag(I) uptake (12 h)

a)

b)
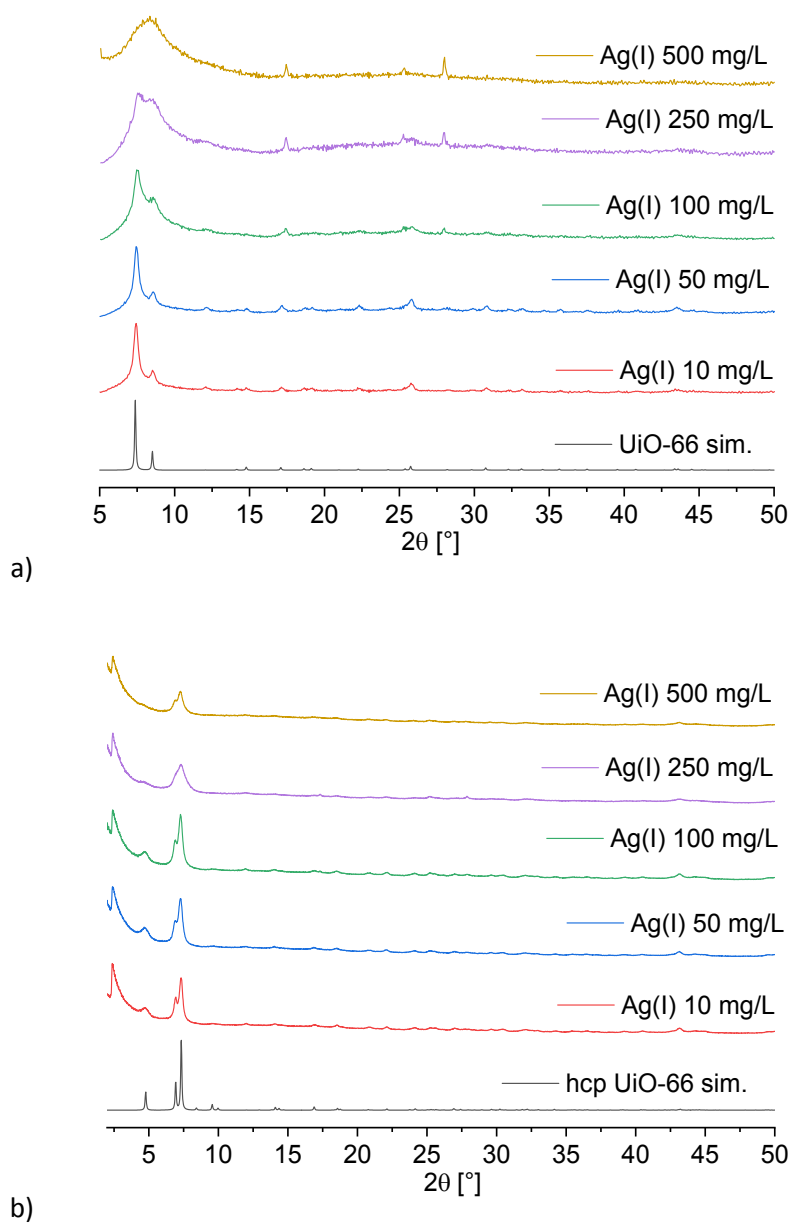
Figure S50 PXRD pattern of (a) UiO-66-MAc-50eq and (b) UiO-66-MAc-100eq after Ag(I)-uptake (12 h) with Ag(I) start concentrations of 10, 50, 100, 250 and 500 mg/L and simulated diffractogram of **fcu** UiO-66 (from cif file CCDC837796) and **hcp** UiO-66 (from cif file CSD-Refcode: KINGUM).[5, 7]

S13.1.2 N$_2$-sorption isotherms (at 77K) of UiO-66-MAc-50eq and -100eq after Ag(I) uptake (12 h)

Nitrogen-sorption isotherms of the MOFs after the Ag(I) uptake experiments showed a significant loss in BET surface area (Fig. S51, Table S8) which is expected and consistent with the intended pore filling. Still, both MOFs retained the same curvature of the isotherms and hysteresis than before the uptake.
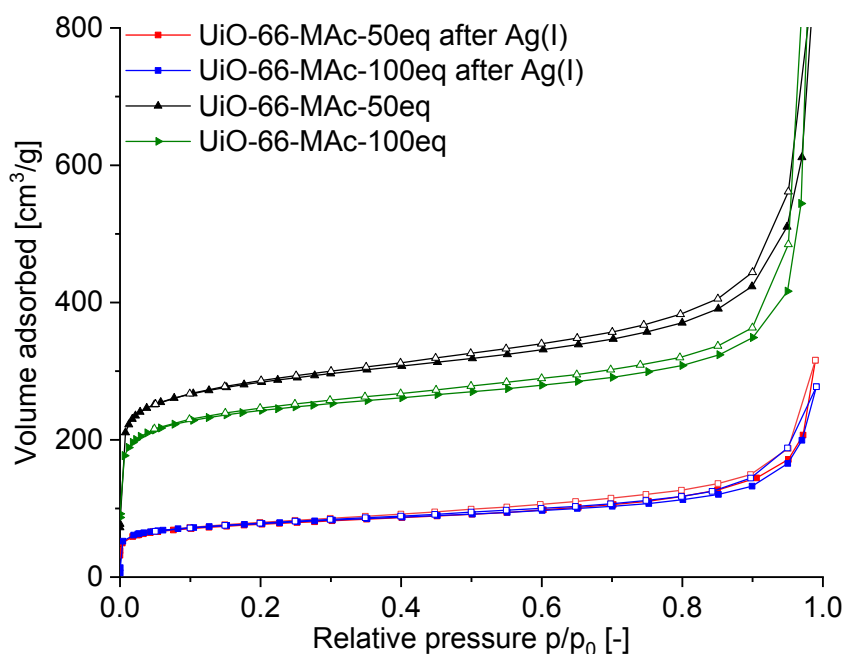
Figure S51 N$_2$-sorption isotherm of UiO-66-MAc-50eq and -100eq at 77 K after the uptake of Ag(I) over 12h in comparison to the isotherms before Ag(I) uptake. Filled symbols: adsorption; empty symbols: desorption.

Table S8 Porosity characteristics of UiO-66-MAc-50eq and -100eq before and after Ag(I) uptake

Material	S$_{BET}$[a]	A$_{Int}$[b]	A$_{Ext}$[c].
UiO-66-MAc-50eq before Ag(I)	1072	825	247
UiO-66-MAc-50eq after Ag(I)	282	167	115
UiO-66-MAc-100eq before Ag(I)	912	708	204
UiO-66-MAc-100eq after Ag(I)	278	157	121

[a] Multi-Point BET between p/p$_0$ = 0.01 - 0.05. [b] Internal micropore surface area determined from t-plot and V-t method. [c] External surface area, i.e., the surface area from meso- and macropores, determined from t-plot and V-t method.

**S13.1.3 X-ray photoelectron spectroscopy (XPS) of UiO-66-MAc-50eq and -100eq after Ag(I) uptake (12 h)**

X-ray photoelectron spectroscopy (XPS) was performed in order to investigate the surface composition and the chemical state of the Ag for UiO-66-MAc-50eq and UiO-66-MAc-100eq. The survey spectra in Figure S52a (UiO-66-MAc-50eq) and 52c (UiO-66-MAc-100eq) confirm the presence of C, O, S, Ag and Zr for both materials.

The high-resolution Ag 3d XPS spectrum of UiO-66-MAc-50eq in Figure S52b displays the main core peaks at 368.2 eV and 374.1 eV that are assigned to Ag $3d_{5/2}$ and Ag $3d_{3/2}$ respectively. Peak positions together with the 6 eV doublet splitting indicates the metallic state of Ag(0).[13] Another spin-orbit pair with higher binding energies at 369.4 eV and 375.4 eV for Ag $3d_{5/2}$ and Ag $3d_{3/2}$ respectively is attributed to the silver(I) atoms bonding with thiol groups (Ag-S-R). The ratio of Ag(0):Ag(I) is about 10:1. The high resolution Ag 3d XPS spectrum of UiO-66-MAc-100eq in Figure S52d shows similarly two main peaks at 368.3 eV and 374.3 eV for Ag $3d_{5/2}$ and Ag $3d_{3/2}$ respectively that are indicative for metallic Ag(0), whereas the peaks at 369.2 eV and 375.2 eV are again assigned to silver(I) ions bonding with thiol groups.[13,14] Here, the molar Ag(0):Ag(I) ratio is about 3:1.

The results indicate primarily the reduction of Ag(I) to Ag(0) under oxidation of the thiols to the aforementioned S-S disulfide (Section S3) as described in the literature.[15] These results are in accordance to Raman spectra and ^{1}H-NMR spectra which showed signals assignable to the disulfide. Some Ag$^+$ ions are chemisorbed through the formation of R-S-Ag bonds to the thiol groups.
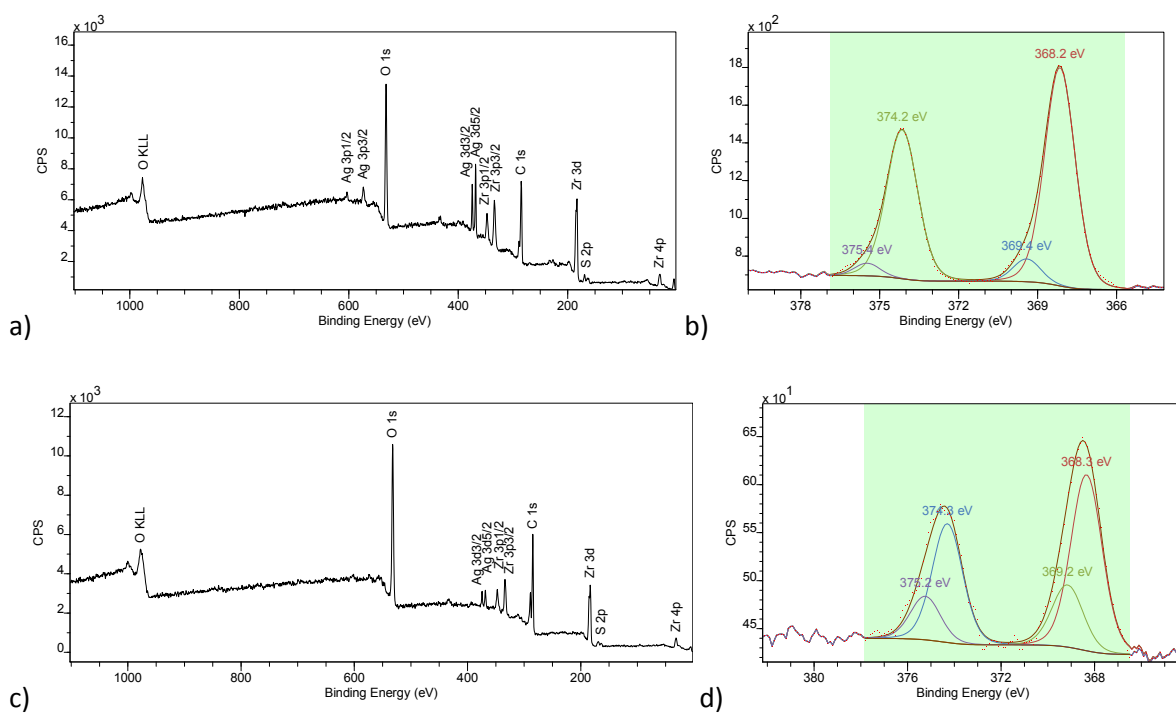
Figure S52 Survey XPS spectra for (a) UiO-66-50eq and (c) UiO-66-100eq (c) and high resolution XPS spectra of Ag 3d for (b) UiO-66-MAc-50eq and (d) UiO-66-MAc-100eq.

S13.2 SEM-EDX mappings for UiO-66-MAc-50eq and UiO-66-MAc-100eq after Ag(I) uptake (12 h; Ag(I) start concentration 500 mg/L)
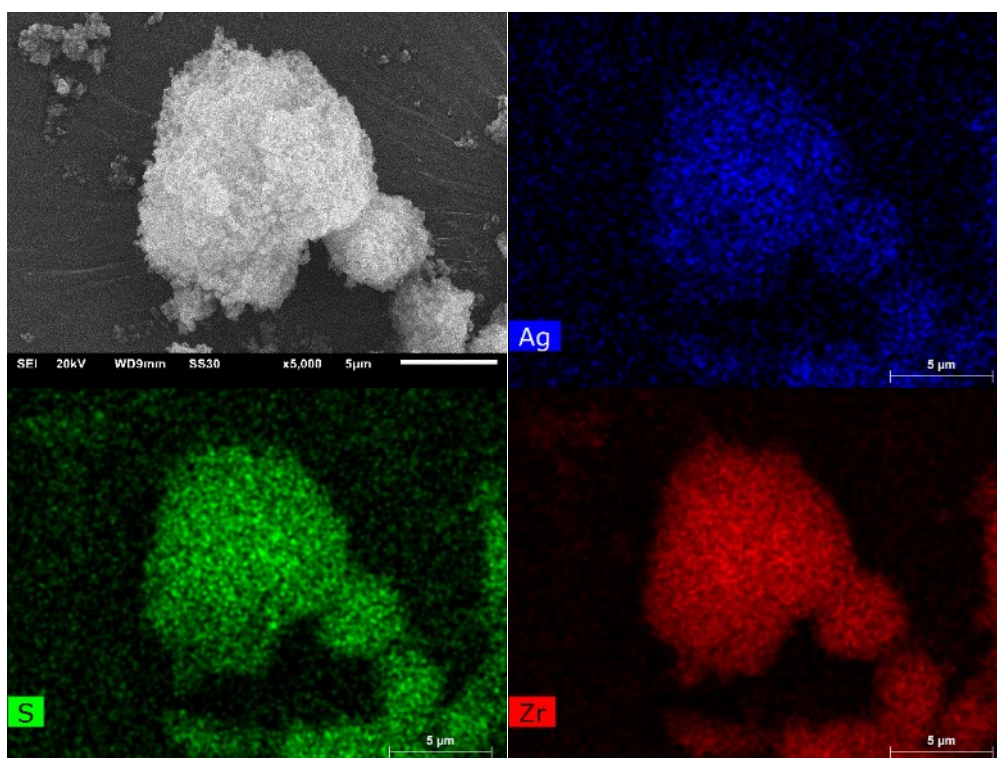
Figure S53 SEM image of UiO-66-MAc-50eq after 12 h Ag(I)-uptake (start concentration Ag(I) 500 mg/L) and its Zr (red), S-(green) and Ag (blue) EDX elemental maps.
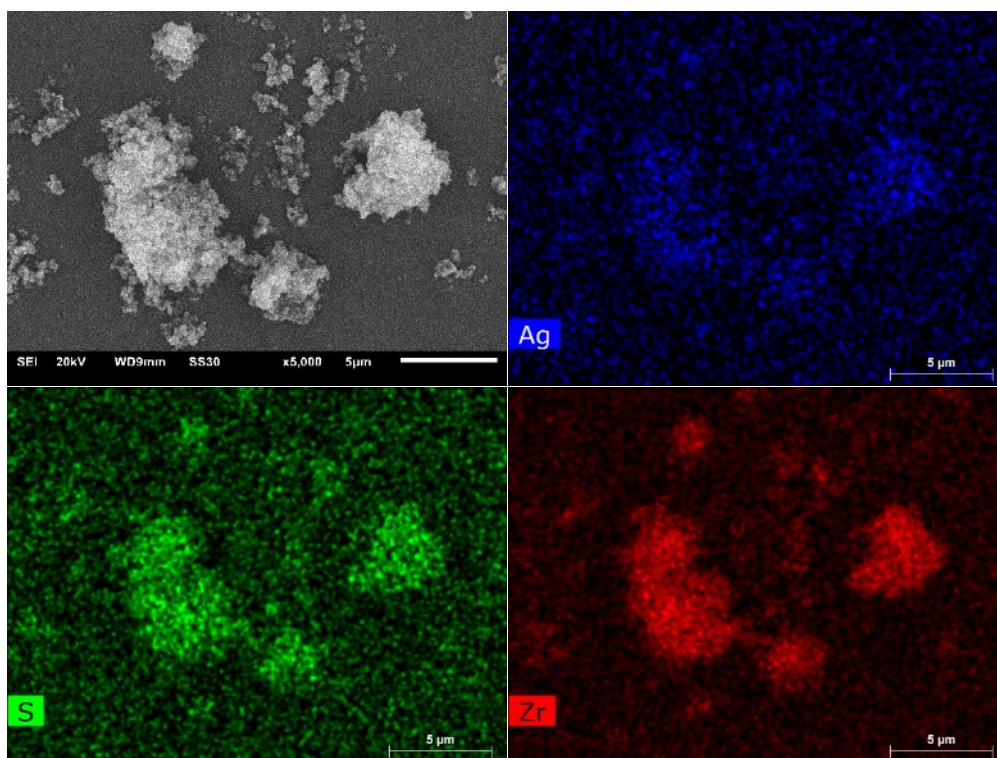
Figure S54 SEM image of UiO-66-MAc-100eq after 12 h Ag(I) uptake (start concentration Ag(I) 500 mg/L) and its Zr (red), S-(green) and Ag (blue) EDX elemental maps.

S13.3.1 Regeneration after Ag(I) uptake with KCN

The regeneration with KCN was tested, to see if a recycling of the MOFs after Ag uptake was possible. For the regeneration samples were shaken in KCN solution for 24 h. For quantification of the effect of aqueous KCN solution on the silver amount after the uptake experiments, SEM-EDX and PXRD were used. Samples were prepared as described for the silver ion removal studies. Results are presented in Table S8.

SEM-EDX mappings showed uniform distribution of signals, which is referred to background noise. No higher concentrations of silver were detected on or near the MOF particles (Fig. S43 and S44). EDX measurements showed a strong decrease in the silver concentration after the regeneration experiment (Table S9). PXRD measurements showed a strong decrease in crystallinity for both MOFs after the extraction of silver (Fig. S56).
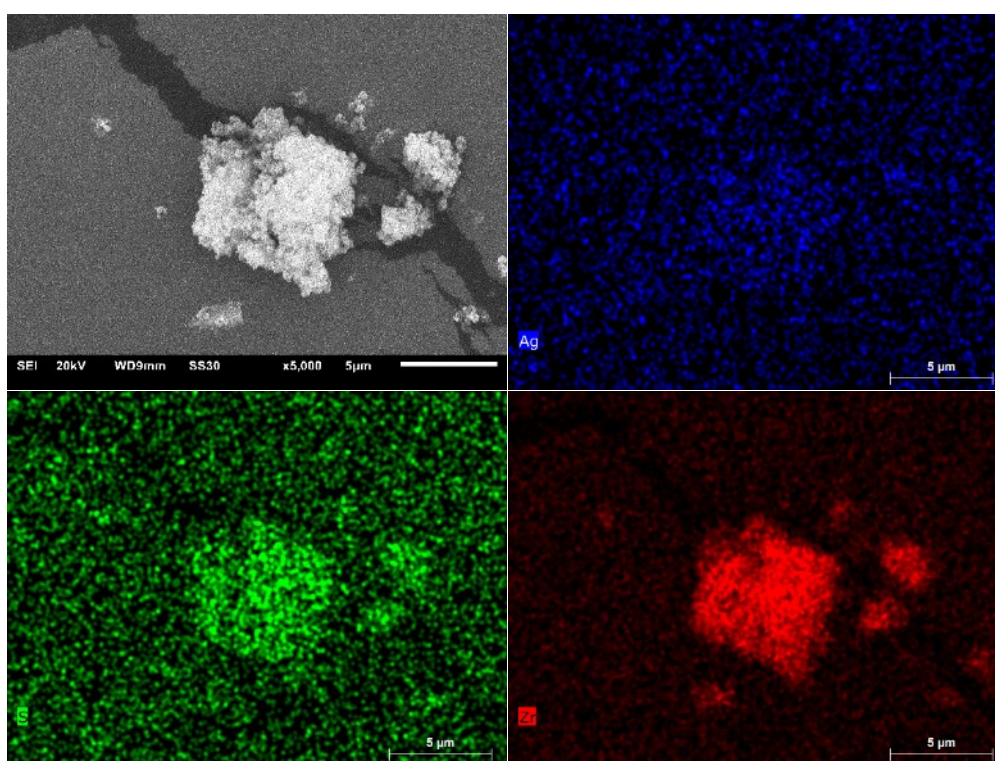
Figure S55 SEM-picture of UiO-66-MAc-50eq after 24 h regeneration with KCN solution (in water, concentration 500 mg/L) and its Zr (red), S-(green) and Ag (blue) EDX elemental maps.
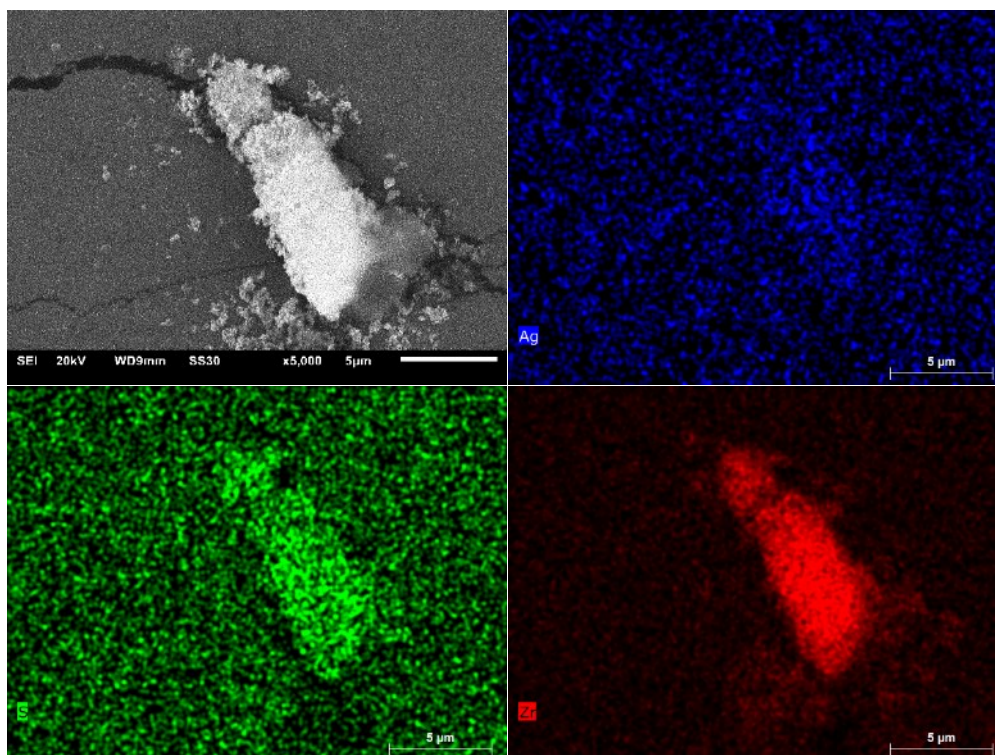
Figure S56 SEM-picture ofUiO-66-MAc-100eq after 24 h regeneration with KCN solution (in water, concentration 500 mg/L) and its Zr (red), S-(green) and Ag (blue) EDX elemental maps.

Table S9 Atom% of silver after Ag(I) uptake and after regeneration with KCN determined by SEM-EDX.

Material	Ag after uptake experiment [At%]	Ag after regeneration experiment [At%]
UiO-66-MAc-50eq	0.44 ± 0.10	0.05 ± 0.04
UiO-66-MAc-100eq	0.15 ± 0.06	0

(a)

(b)
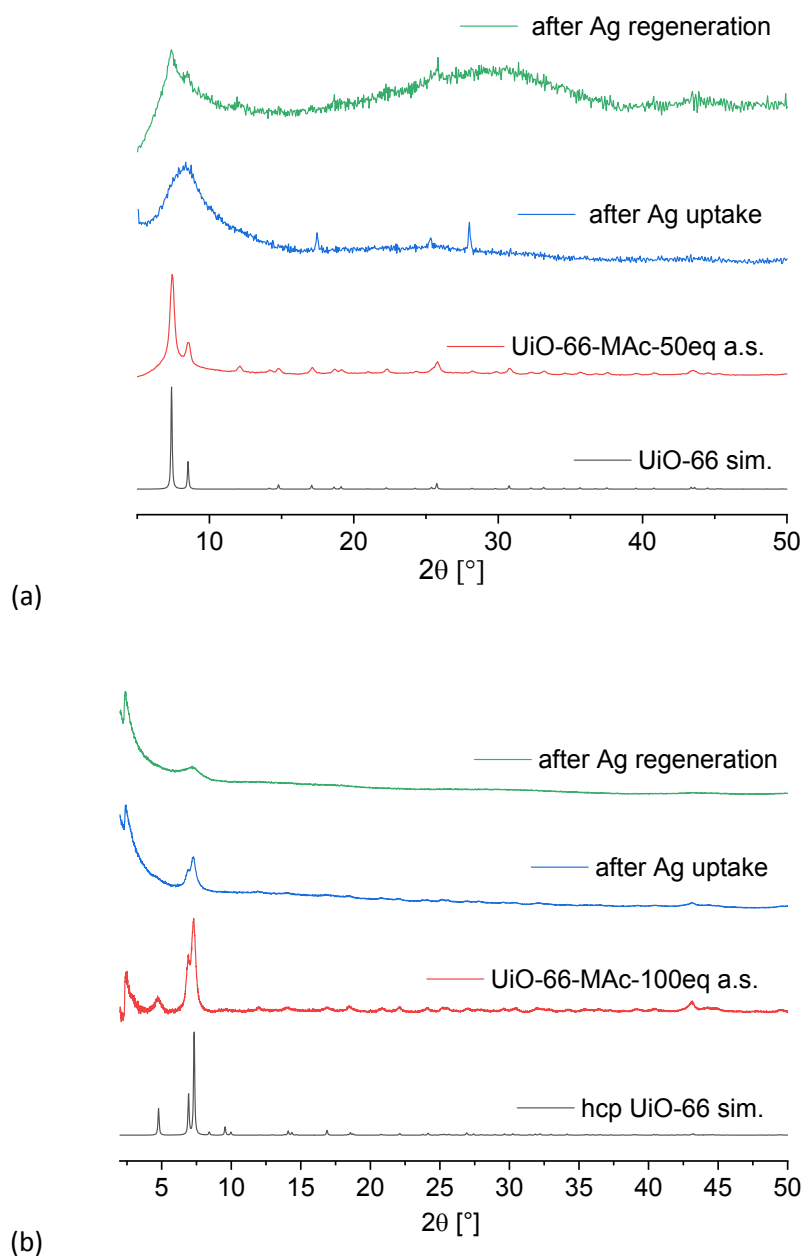
Figure S57 PXRD pattern of UiO-66-MAc-50eq (a) and UiO-66-MAc-100eq (b) after regeneration experiments with KCN (24 h) and simulated diffractogram of UiO-66 (from cif file CCDC837796) and **hcp** UiO-66 (from cif file CSD-Refcode: KINGUM).[5, 7]

S13.3.2 N$_2$-sorption isotherms (at 77K) of UiO-66-MAc-50eq and -100eq after regeneration experiments

Nitrogen-sorption isotherms of the MOFs after the regeneration experiments with KCN showed a significant loss in BET surface area (Fig. S58, Table S10). Attempted regeneration of the MOFs resulted in significant damage to the crystalline structure as evidenced by the PXRD pattern (Fig. S57) and the nearly complete loss of the original BET surface area. Still, both "regenerated" MOFs retained the same curvature of the isotherms and hysteresis than before the uptake.
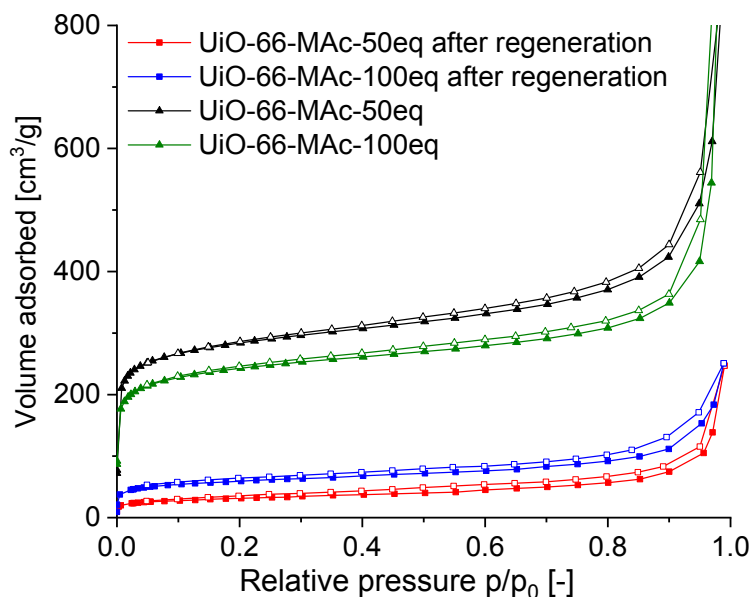
Figure S58 N$_2$-sorption isotherm of UiO-66-MAc-50eq and -100eq at 77K after regeneration experiments with KCN (24 h) in comparison to the isotherms before Ag(I) uptake. Filled symbols: adsorption; empty symbols: desorption.

Table S10 Porosity characteristics of UiO-66-MAc-50eq and -100eq before Ag uptake and after Ag(I) regeneration with KCN

Material	S$_{BET}$[a]	A$_{Int}$[b]	A$_{Ext}$[c]
UiO-66-MAc-50eq	1072	825	247
UiO-66-MAc-50eq after regen.	112	48	63
UiO-66-MAc-100eq	912	708	204
UiO-66-MAc-100eq after regen.	217	53	164

[a] Multi-Point BET between p/p$_0$ = 0.01 - 0.05. [b] Internal micropore surface area determined from t-plot and V-t method. [c] External surface area, i.e., the surface area from meso- and macropores, determined from t-plot and V-t method.

S14 Investigation on the transition of fcu UiO-66-MAc to To further investigate the transition of the **fcu** UiO-66 to the **hcp** UiO-66 structure by incorporation of the MAc modulator, additional MOF syntheses with 70, 80 and 90eq modulator in relation to $ZrCl_4$ were carried out. Figure S58 shows the PXRD patterns in comparison with the **hcp** UiO-66-MAc-100eq MOF and the simulated PXRD patterns for **fcu** UiO-66 and **hcp** UiO-66. With 70eq in relation to $ZrCl_4$ the structure remains of **fcu** type. UiO-66-MAc-80eq shows the **hcp** reflexes but with poorer crystallinity than the -90eq and -100eq MOFs. The reflexes of UiO-66-Mac-90eq are already in good accordance with the simulated diffractogram of **hcp** UiO-66. Thus, above 70eq of modulator in relation to the metal salt the **fcu** structure changes towards the **hcp** structure. At the modulator amounts of 70eq and 80eq the product crystallinity is generally low. This may be due to the formation of both **fcu** and **hcp** phase albeit in small and not well-developed crystallites. The use of 90eq of modulator showed yielded the **hcp** structure of UiO-66.
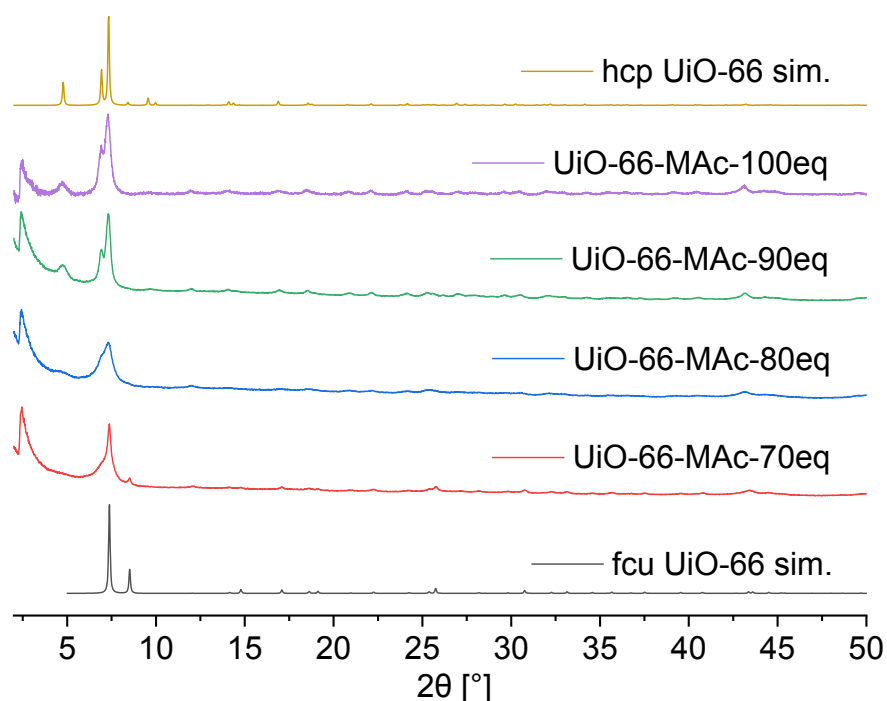
Figure S59 PXRD pattern of UiO-66-MAc-70eq, -80eq, -90eq and -100eq and simulated diffractogram of **fcu** UiO-66 (from cif file CCDC837796) and **hcp** UiO-66 (from cif file CSD-Refcode: KINGUM).[5,7]

S15 Literature overview for the removal of Ag(I) from aqueous solution

Table S11 presents a short literature overview on the removal of silver ions and silver nanoparticles from aqueous solution, comparing the maximum uptake and the adsorption mechanism. Because of the high variety of different materials and composites tested for the uptake of silver, this comparison only shows a small overview of the wide array of materials with the capability for removing silver from aqueous solution.

Table S11 Literature overview of materials used for the removal of Ag(I) ions and siler nanoparticles from aqueous solution.

Material	Maximum uptake (Ag)I in [mg/g]	Adsorption model	Reference
fcu UiO-66-MAc-50eq	84	Langmuir/ chemisorption	This work
hcp UiO-66-MAc-100eq	36	Langmuir/ chemisorption	This work
UiO-66-NH$_2$-Rd[a]	163	Freundlich or Redlich-Peterson/ chemisorption	[16]
HKUST-1[b]	80	Freundlich / physisorption	[17]
Amine-based COF[c]	175	Langmuir/ chemisorption	[18]
Fe$_3$O$_4$@SiO$_2$@TiO$_2$-IIP[d]	35	Langmuir/ chemisorption	[19]
MgAl-MoS$_4$-LDH[e]	450	Langmuir/ chemisorption	[20]
Fe$_3$O$_4$/PPy[f]	143	Langmuir/ chemisorption	[21]
Ag-IIPs[g]	81	Langmuir/ chemisorption	[22]
AC/γ-Fe$_2$O$_3$-BPDM[h]	33	Langmuir/ chemisorption	[23]
EP[i]	8	Langmuir/ chemisorption	[24]
Magnetic chitosan resin[j]	227	Langmuir/ chemisorption	[25]

[a] Rd = rhodanine,[16], Freundlich and Redlich-Peterson models produced nearly similar R^2; - [b] Cu-BTC, copper-based metal organic framework,[17] uptake of silver nanoparticles; - [c] COF = covalent organic framework;[18] - [d] IIP = ion-imprinted polymer;[19] - [e] LDH = layered double hydroxide;[20] - [f] PPy = polypyrrole, forming a magnetic nanocomposite;[21] - [g] IIP = ion-imprinted particles;[22] - [h] AC/ γ-Fe$_2$O$_3$= activated carbon/ γ-Fe$_2$O$_3$ composite (magnetical), BPDM= 4,4'-bis-(3-phenylthiourea)diphenyl methane;[23] - [i] EP = expanded perlite (amorphous volcanic glass);[24] - [j] magnetite, thiourea and glutaraldehyde modified chitosan resin.[25]

References

[1] J. Srogl, W. Liu, D. Marshall and L. S. Liebeskind. *J. Am. Chem. Soc.*, 1999, **121**, 9449-9450.

[2] S. Lim, M. Ji, X. Wang, C. Lee and H.-Y. Jang, *Eur. J. Org. Chem.*, 2015, **3**, 591-595.

[3] T. J. Wallace and A. Schriesheim, *J. Org. Chem.*, 1962, **27**, 1514-1516.

[4] G. C. Shearer, S. Chavan, S. Bordiga, S. Svelle, U. Olsbye and K. P. Lillerud, *Chem. Mater.*, 2016, **28**, 3749-3761.

[5] M. Ermer, J. Mehler, M. Kriesten, Y. S. Avadhut, P. S. Schulz and M. Hartmann, *Dalton Trans.*, 2018, **47**, 14426-14430.

[6] J. H. Cavka, S. Jakobsen, U. Olsbye, N. Guillou, C. Lamberti, S. Bordiga and K. P. Lillerud, *J. Am. Chem. Soc.*, 2008, **130**, 13850-13851.

[7] R. Dalapati, B. Sakthivel, A. Dhakshinamoorthy, A. Buragohain, A. Bhurnia, C. Janiak and S. Biswas, *CrystEngComm*, 2016, **18**, 7855-7864.

[8] L. Valenzano, B. Civalleri, S. Chavan, S. Bordiga, M. H. Nilsen, S. Jakobsen, K. P. Lillerud and C. Lamberti, *Chem. Mater.*, 2011, **23**, 1700-1718.

[9] P. Yang, Y. Shu, Q. Zhuang, Y. Li and J. Gu, *Chem. Commun.*, 2019, **55**, 12972-12975.

[10] B. Subramanyam and A. Das, *J. Environ. Health Sci.*, 2014, **12**, 92.

[11] P. Yang, Y. Shu, Y. Li and J. Gu, *Langmuir*, 2019, **35**, 16226-16233.

[12] J. Lin and L. Wang, *Front. Environ. Sci. Engin. China*, 2009, **3**, 320-324.

[13] X. Cheng, M. Liu, A. Zhang, S. Hu, C. Song, G. Zhang and X. Guo, *Nanoscale*, 2015, **7**, 9738-9745.

[14] C. Battocchio, I. Fratoddi, L. Fontana, E. Bodo, F. Porcaro, C. Meneghini, I. Ois, S. Nappini, S. Mobilio, M. V. Russo and G. Polzonetti, *Phys. Chem. Chem. Phys.*, 2014, **16**, 11719-11728.

[15] L. Liu, C. A. Burnyeat, R. S. Lepsenyi, I. O. Nwabuko and T. L. Kelly, *Chem. Mater.*, 2013, **25**, 4206-4214.

[16] L. Ding, P. Shao, Y. Luo, X. Yin, S. Yu, L. Fang, L. Yang, J. Yang and X. Luo, *Chem. Eng. J.*, 2020, **382**, 123009.

[17] J. E. Conde-González, E. M. Peña-Méndez, S. Rybáková, J. Pasán, C. Ruiz-Pérez and J. Havel, *Chemosphere*, 2016, **160**, 659-666.

[18] L. Wang, M. Deng, H. Xu, W. Li, W. Huang, N. Yan, Y. Zhou, J. Chen and Z. Qu, *ACS Appl. Mater. Interfaces*, 2020, **12**, 37619-37627.

[19] X. Yin, J. Long, Y. Xi and X. Luo, *ACS Sustainable Chem. Eng.*, 2017, **5**, 2090-2097.

[20] L. Ma, Q. Wang, S. M. Islam, Y. Liu, S. Ma and M. G. Kanatzidis, *J. Am. Chem. Soc.*, 2016, **138**, 2858-2866.

[21] X. Peng, W. Zhang, L. Gai, HJ. Jiang, Y. Wang and L. Zhao, *Chem. Eng. J.*, 2015, **280**, 197-205.

[22] H. Hou, D. Yu and G. Hu, *Langmuir*, 2015, **31**, 1376-1384.

[23] M. Ghanei-Motlagh, M. Fayazi, M. A. Taher and A. Jalalinejad, *Chem. Eng. J.*, 2016, **290**, 53-62.

[24] H. Ghassabzadeh, A. Mohadespour, M. Torab-Mostaedi, P. Zaheri, M. Ghannadi Maragheh and H. Taheri, *J. Hazard. Mater.*, 2010, **177**, 950-955.

[25] A. M. Donia, A. A. Atia and K. Z. Elwakeel, *Hydrometallurgy*, 2007, **87**, 197-206.